JOURNAL OF GEOPHYSICAL RESEARCH, VOL. 105, NO. B6, PAGES 13,905–13,931, JUNE 10, 2000

Seismovolcanic signals at Deception Island volcano, Antarctica: Wave field analysis and source modeling

Jesús M. Ibáñez,[1,2] Edoardo Del Pezzo,[3] Javier Almendros,[1,4] Mario La Rocca,[3,5] Gerardo Alguacil,[1,2] Ramón Ortiz,[6] and Alicia García[6]

Abstract. The seismovolcanic signals associated with the volcanic activity of Deception Island (Antarctica), recorded during three Antarctic summers (1994-1995, 1995-1996 and 1996-1997), are analyzed using a dense small-aperture (500 m) seismic array. The visual and spectral classification of the seismic events shows the existence of long-period and hybrid isolated seismic events, and of low-frequency, quasi-monochromatic and spasmodic continuous tremors. All spectra have the highest amplitudes in the frequency band between 1 and 4 Hz, while hybrids and spasmodic tremors have also significant amplitudes in the high-frequency band (4-10 Hz). The array analysis indicates that almost all the well-correlated low-frequency signals share similar array parameters (slowness and back azimuth) and have the same source area, close to the array site. The polarization analysis shows that phases at high-frequency are mostly composed of P waves, and those phases dominated by low frequencies can be interpreted as surface waves. No clear shear waves are evidenced. From the energy evaluation, we have found that the reduced displacement values for surface and body waves are confined in a narrow interval. Volcano-tectonic seismicity is located close to the array, at a depth shallower than 1 km. The wave-field properties of the seismovolcanic signals allow us to assume a unique source model, a shallow resonating fluid-filled crack system at a depth of some hundreds of meters. All of the seismic activity is interpreted as the response of a reasonably stable stationary geothermal process. The differences observed in the back azimuth between low and high frequencies are a near-field effect. A few episodes of the degassification process in an open conduit were observed and modeled with a simple organ pipe.

1. Introduction

Deception Island is a volcanic island located at 62°59'S and 60°41'W, northeast of the Antarctic Peninsula (Figure 1). It is considered to be the main active volcano of the back arc basin of the Bransfield Strait [*Baker et al.*, 1975; *Baker*, 1990]. Its last eruption took place in 1970. Several works focused on the study of the seismic activity of Deception Island have been carried out in the last 10 years. First studies were done analyzing data recorded by a seismic network composed of five vertical-component sensors with a 12 bit data acquisition system [e.g., *Vila et al.*, 1992, 1995] during three Antarctic summer surveys (1989-1991). They provide an epicentral map of the seismic activity and interpret some typical volcanic tremors as associated with a mechanism of degassification of an aquifer in contact with hot materials. *Correig et al.* [1997] statistically analyzed the same set of data with a nonlinear approach, suggesting a qualitative source model for the seismic activity, based on the interaction of water and hot materials. *Ortiz et al.* [1997] presented a brief description of the seismic surveys carried out in Deception Island from 1986 to 1994. These authors reported the occurrence of volcano-tectonic (VT), long-period (LP), and volcanic tremor events. Moreover, they described the main characteristics of an intense seismic swarm that took place in the period January-February 1992, with the occurrence of felt VT and tremor events and hundreds of LP events per day. These authors related the signal amplitude variation with the time of the seismic signals to an anomalous gravity change that occurred during the swarm. They proposed three possible qualitative models to explain this observation: (1) density variation in an aquifer, (2) an increase of the heat transfer from the magmatic body to the aquifer, (3) a deep magmatic intrusion. The existence of deep seismic events in the area and a volcano-magnetic effect support the idea of a deep magmatic injection.

The field experience, provided by all the above cited surveys, shows that on average the energy of the seismovolcanic signals recorded since 1988 at Deception volcano is low, with the existence of low-magnitude tectonic and volcanic events. A small-aperture seismic antenna was set up close to the summer Spanish Base "Gabriel de Castilla" (Figure 2) during the Antarctic summer field surveys of 1994-1995, 1995-1996, and 1996-1997, with the main aim of tracking the seismovolcanic source. The use of seismic antennas allows us to obtain a complete analysis of the seismic wave field, giving useful information on the nature of the volcanic tremor and of the long-period events that usually characterize the volcano seismicity. Preliminary reports about these array-recorded data [*Alguacil et*

[1]Instituto Andaluz de Geofísica, Universidad de Granada, Granada, Spain.
[2]Also at Departamento de Física Teórica y del Cosmos, Universidad de Granada, Granada, Spain.
[3]Osservatorio Vesuviano, Napoli, Italy.
[4]Now at U.S.G.S., Menlo Park, California, USA.
[5]Also at Dipt. Di Fisica, Universitá di Salerno, Salerno, Italy.
[6]Museo Nacional de Ciencias Naturales, Dpto. Volcanología, Madrid, Spain.

Paper number 2000JB900013.
0148-0227/00/2000JB900013$09.00

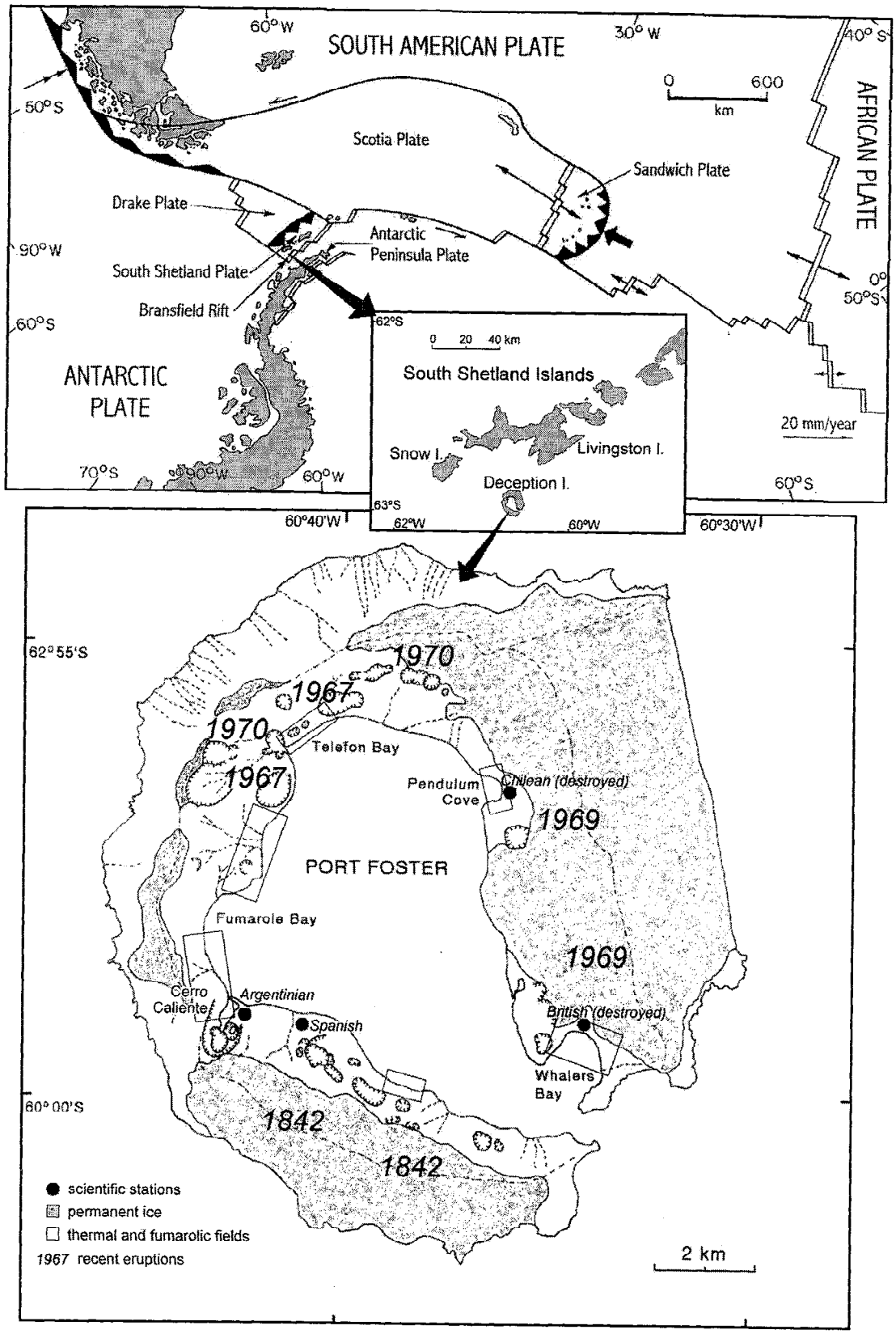

Figure 1. Map of the Deception Island region, showing regional tectonics, geographical position in the South Shetland Islands, main topographic features, historical eruptions, and thermal and fumarolic fields.

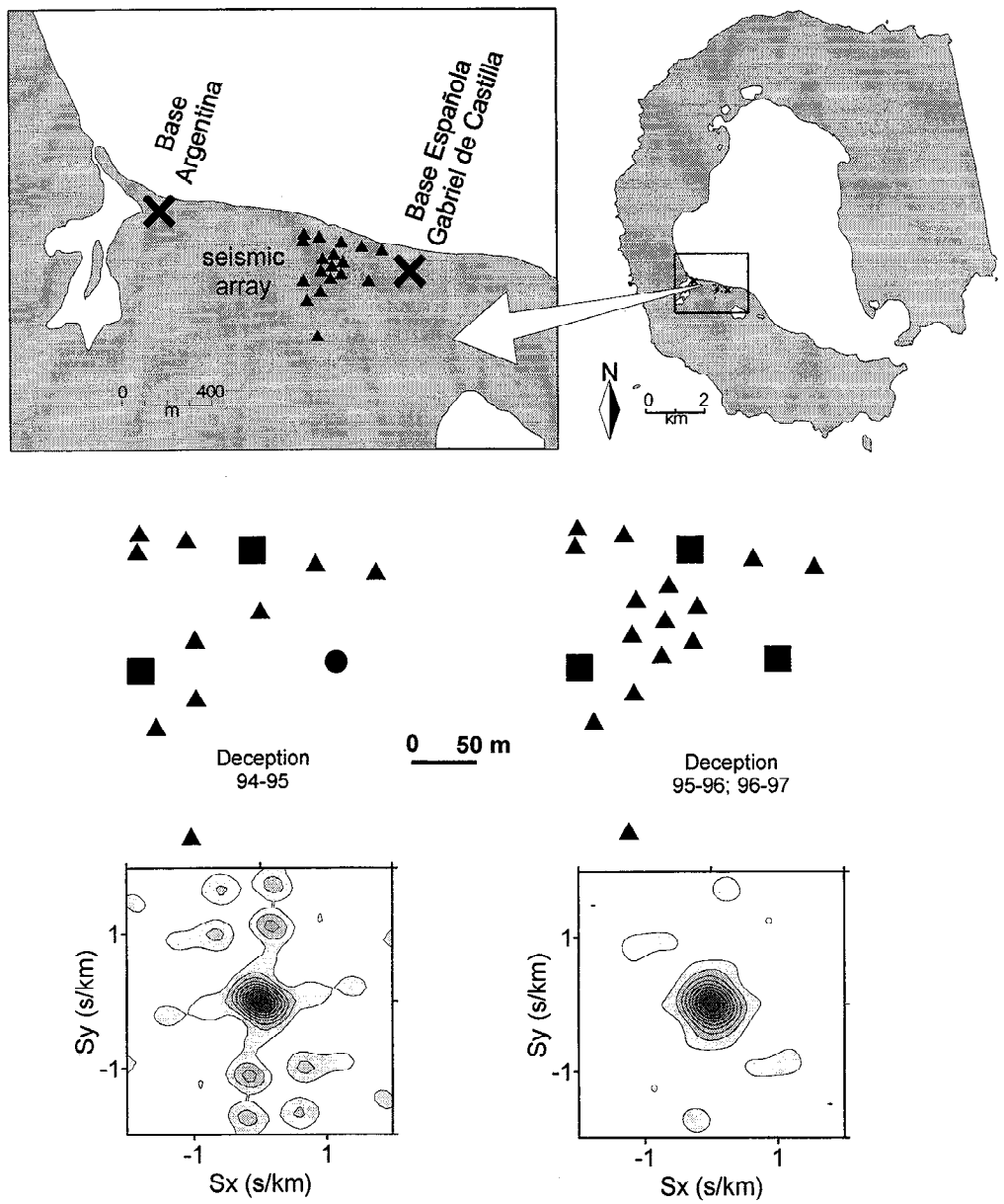

Figure 2. Location and configuration of the seismic antennas used in the three field experiments. Triangles mark the location of vertical seismometers (Mark L25B), squares mark the position of 3-D Mark L-4C stations, and dots show the broadband station site, used in the first survey. At the bottom of the figure, the beam-pattern resolution of both configurations is shown at 2 Hz.

al., 1999] confirmed the existence of VT, LP, and sustained tremor events with a location close to the array area. First analyses [*Almendros et al.*, 1997] show that some volcanic tremor episodes are generated by the multiple occurrences of low-energy LP events and report the presence of intermediate depth (30-120 km) and shallow earthquakes (0-30 km) in the area [*Ibáñez et al.*, 1997a]. *Almendros et al.* [1999] introduced a modification of the zero lag cross-correlation technique taking into account the circular geometry of the incoming wave fronts. Using this technique, they determined the epicentral coordinates of a subset of seismovolcanic long-period events, which occurred close to the array.

Array data analyses in slowness space, combined with the evaluation of the polarization properties of the wave field, increase the level of information that is usually obtained from conventional seismic networks. The use of dense and small aperture seismic antennas allows one, in fact, to track (spatially and temporally) the source of the sustained tremor and long-period events, even in the case of very emergent first onset. Many studies have been carried out with this aim at different volcanoes, such as Stromboli [*Chouet et al.*, 1997; *Saccorotti et al.*, 1998], Kilauea [*Ferrazzini et al.*, 1991; *Goldstein and Chouet*, 1994], Teide [*Del Pezzo et al.*, 1997; *Almendros et al.*, 2000] Masaya [*Metaxian et al.*, 1997], or Deception Island [*Ibáñez et al.*, 1997b; *Almendros et al.*, 1997].

The aim of the present study is to improve our understanding of the seismovolcanic processes occurring at the Deception Island volcano, using the complete set of data recorded during the Antarctic field surveys in which the small-aperture array has been in operation (1994-1997). We first classify the seismic events on the basis of their spectral properties, without taking into account the source processes involved. Then we investigate the properties

of the wave field generated by the different types of seismic events using array and polarization techniques, in order to estimate their energy, back azimuth, apparent slowness, and wave composition. The results are interpreted in terms of a fluid-filled resonant crack excited by a pressure step.

2. Geology and Eruptive History

Deception, Bridgeman, and Penguin Islands are the three main active volcanic islands in the South Shetland Islands and Antarctic Peninsula. Their geodynamics is typical of a rift framework (the Bransfield Rift; see Figure 1 for details). Deception Island is located astride a Quaternary marginal basin-spreading center in the Bransfield strait [*Smellie*, 1988], which separates the South Shetland Islands from the Antarctic Peninsula. Deception is a horseshoe-shaped volcano with a submerged basal diameter of 25 km and a 15 km diameter of the emerged structure. The known eruptions took place in 1842, 1967, 1969, and 1970; two eruptions (1912 and 1917) have been dated with great uncertainty [*González-Ferrán*, 1995; *De Rosa et al.*, 1995]. During the 1969 eruption, two permanent bases of the island were destroyed (Chilean by pyroclastic flows and British by a surge). *Roobol* [1979] provides a partial reconstruction of the eruptive history of Deception from 1829, including other possible eruptions. An important eruption that occurred in the 17th century was deduced by the ice record in James Ross Island, 200 km from Deception [*Aristarain and Delmas*, 1998]. They deduced that probably this eruption had been the largest one on the island in the last 350 years. *Casertano* [1967] provides an interesting report of the geological and geophysical features before the 1969 eruption. During eruptions, at least in the last 100 years, a limited amount of magma and volatile materials is produced, with a duration from a few hours to several days. The primary style of eruption is Strombolian, which ends with viscous lava flows, as in 1969. Another style is phreatomagmatic, which occurred, for instance, in the 1970 eruption. A map of the site of the main eruptions and the most important geological features is reported in Figure 1.

Petrologic and volcanological studies [*Smellie*, 1988, 1989; *Smellie et al.*, 1988] suggest the presence of a caldera structure, which resulted from the collapse of several preexisting volcanic structures [*Hawkes*, 1961] or from a central stratovolcano [*Gonzalez-Ferrán and Katsui*, 1970; *Baker et al.*, 1975]. An important feature of Deception is the presence of many shallow aquifers, deduced by the observed hydrothermal alteration [*Martí and Baraldo*, 1990] and by the study of the chemical composition of fumaroles and thermal springs [*Martini and Giannini*, 1988]. These authors infer from thermodynamic considerations that temperatures of 600°C can be reached at a depth of a few kilometers.

Fumarolic emissions and thermal springs are located on the principal fracture crossing the island in a NE-SW direction (Fumarole Bay to Pendulum Cove). The maximum temperature (110°C) of the emission is registered in Fumarole Bay. Other minor emissions are in Telefon and Whalers Bays. The highest ground surface temperature is 130°C in Cerro Caliente (Figure 1).

3. Field Surveys and Instruments

During the austral summers of 1994-1997, three field surveys were carried out deploying a dense short-period seismic antenna. The seismic antenna was set up near the Spanish Base (Figure 2). In the first survey the array was composed of 10 vertical and three three-dimensional (3-D) seismometers. In the other two experiments, 15 vertical and three 3-D seismometers were deployed. The vertical seismometers were Mark L25, with a natural frequency at 4.5 Hz. Their response was electronically extended to 1 Hz. The 3-D seismometers were Mark L-4C with a natural frequency of 1 Hz and electronically extended to 0.1 Hz. In the 1994-1995 experiment, one of the 3-D stations was a Guralp CMG-3 broadband with a flat response between 0.033 and 50 Hz. In Figure 3 we show the overall response curve of the equalized sensors which were pre-amplified at the same level. The preamplifier output is balanced so that the signal is sent undisturbed via twisted pair cables to the data acquisition system, one for each module. Three of such modules composed the whole seismic antenna. Each data acquisition module is composed of an eight channel anti-alias Butterworth multipole filter at 48 Hz; a multiplexer that samples each of the eight channels every 5 ms and a 16 bit A/D converter.

The internal clock is synchronized by GPS time every second, and the sampling rate used is 200 samples per second. The control of each module and the storage of the data are done by a portable PC. The triggering algorithm is based on the STA/LTA ratio. Station Cartesian coordinates were measured with differential GPS positioning. The reference system has the y axis

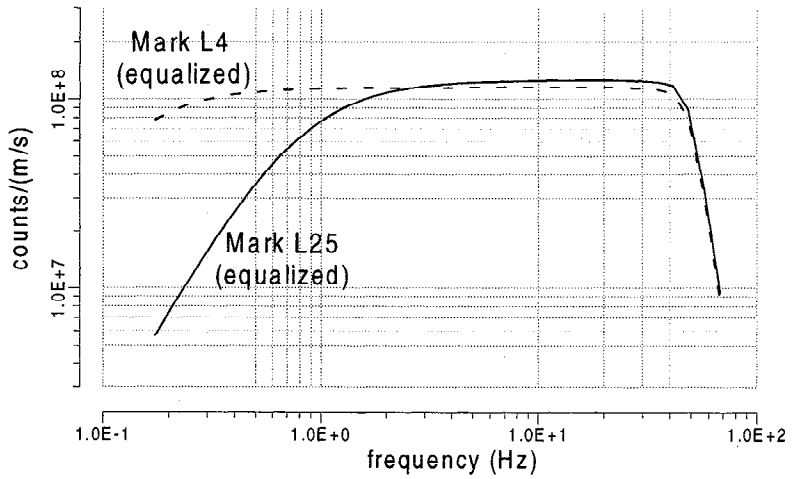

Figure 3. Overall response curve of the equalized sensors used in this work.

oriented toward the north and the x axis toward the east (Figure 2). The array resolution (at 2 Hz) for both configurations used in the present work is reported also in Figure 2. During the 1994-1995 survey a seismic station with continuous recording on paper drum, placed near the Spanish Base, was used for monitoring. In the 1995-1996 and 1996-1997 surveys this station was replaced by a digital, continuously recording PC system.

4. Data Description and Spectral Analysis

In the three field surveys, carried out at Deception Island, the seismic antennas recorded thousands of seismic events. From the whole data set we selected the seismic events that triggered at least two array modules. The daily number of these seismic events during the three periods of observation (the seasons between December and February 1994-1995, 1995-1996 and 1996-1997), is reported in Figure 4. As can be observed, the temporal occurrence is not homogeneous either within the different years or within the same surveys. The seismicity appears clustered in time, with a cluster duration not greater than 5 days. The maximum number of triggers per day took place during the seismic swarm of February 5-9, 1996. We have to point out that during the three surveys analyzed in the present work no visible eruptions occurred in the island.

Seismic records were visually inspected on a computer screen and classified, based on their seismogram shape and on their S-P delay, in regional or local earthquakes, long-period events, or tremor. Inside the long-period event group we could distinguish between pure long-period and hybrid events, following the scheme given by *Lahr et. al.* [1994]. A clear high-frequency and short-duration phase, preceding the arrival of a monochromatic low-frequency signal, characterizes the hybrid event

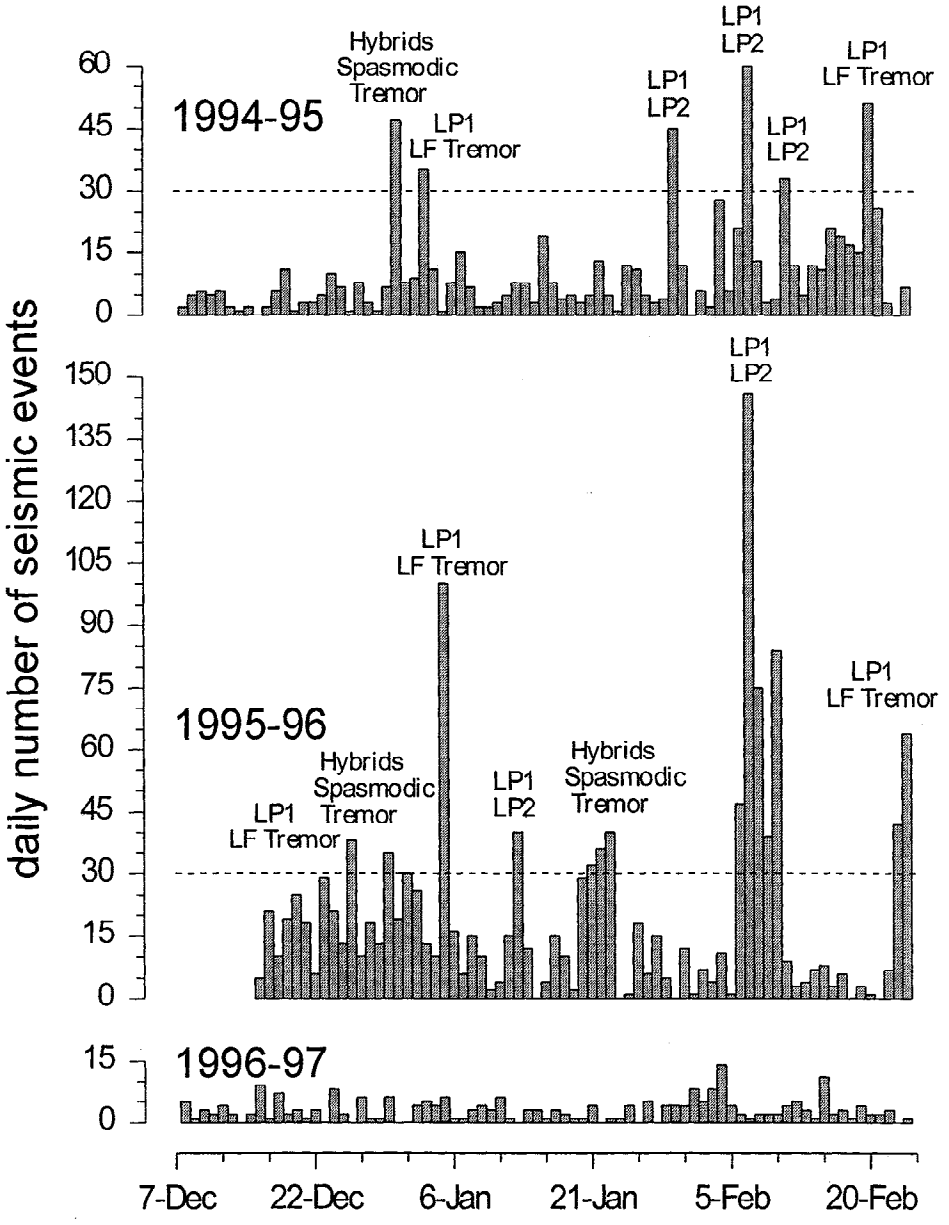

Figure 4. Daily number of triggered events during the three periods of observation. Dashed lines represent the lower limit used to consider the occurrence of a seismic swarm (30 events/day). The dominant type of volcanic events at every seismic swarm is indicated.

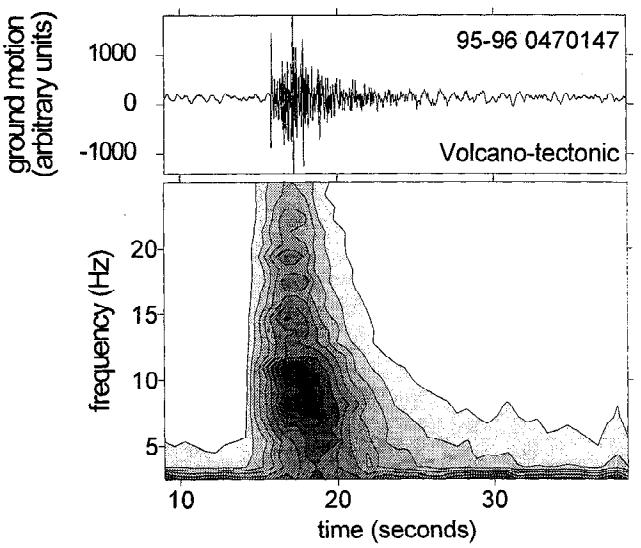

Figure 5. An example of velocity seismograms and array-averaged spectrograms for a volcano-tectonic earthquake. Spectrogram is obtained dividing the vertical digital seismograms into 2.56 s windows, sliding 50 % in time, and averaging over the whole seismic array.

seismograms. After this preliminary visual classification, which is not based on considerations about the source process, we once again reviewed the whole data set with the aid of the spectrogram technique. We divided the digital seismograms into a series of 2.56-s windows (512 samples). The start time of each window was shifted by 256 samples. The spectrum of the ground velocity was evaluated for each window and contoured for the frequency range 0-25 Hz and for the whole duration of the seismogram.

4.1. Regional and Local Earthquakes

The earthquakes with S-P time shorter than 3 s were initially called local earthquakes, because they are located inside the volcanic island. They are characterized by impulsive direct P and S arrivals and by a very broad spectral content, extended up to 30 Hz (Figure 5). A rapid attenuation of the high-frequency peak amplitude with lapse time is clearly observable on the spectrogram. Impulsive P and S direct arrivals characterize the regional earthquakes. Their S-P time is greater than 3 s and their spectral content is broad, ranging between 1 to more than 20 Hz for the direct arrivals.

4.2. Long-Period Events

4.2.1. Pure long-period events. The seismogram envelope for this set of events is fuse-shaped, with a duration between 10 and 60 s. They show a very emergent arrival and an almost pure monochromatic content (Figure 6). Some of these events are preceded by a low-energy and high-frequency phase with a very low signal-to-noise ratio, similar to those described by *Ferrazzini and Aki* [1992]. Three subsets of events can be distinguished according to their predominant spectral peak, LP1, LP2, and LP3, respectively, at 1-2 Hz, 2-3 Hz, and 3-5 Hz. The LP1 events

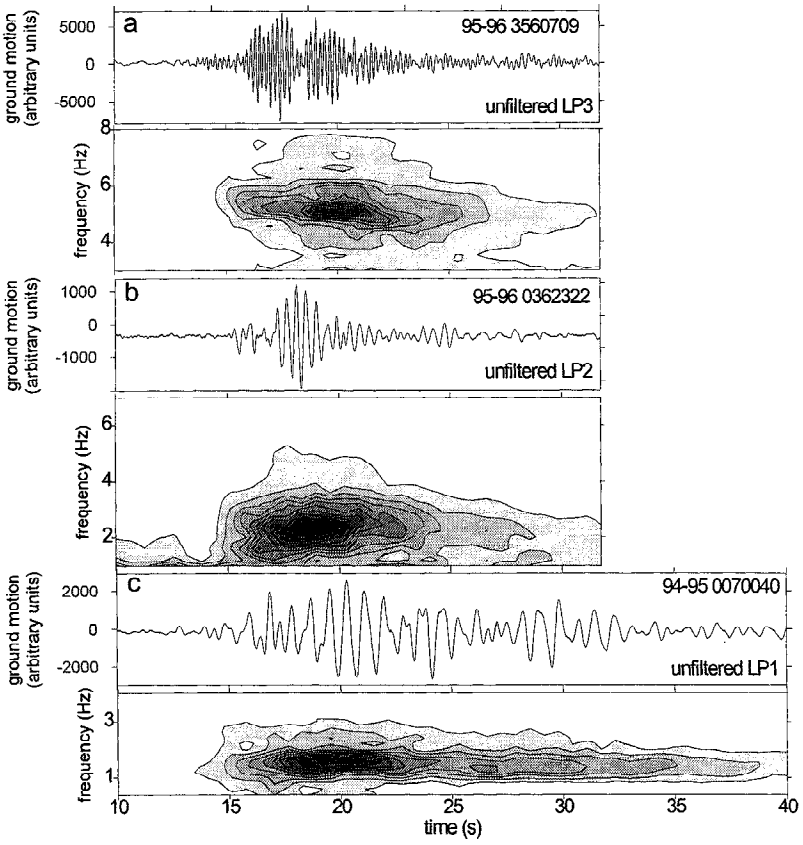

Figure 6. Examples of velocity seismograms and array-averaged spectrograms for (a) LP3 event, (b) LP2 event, and (c) LP1 event.

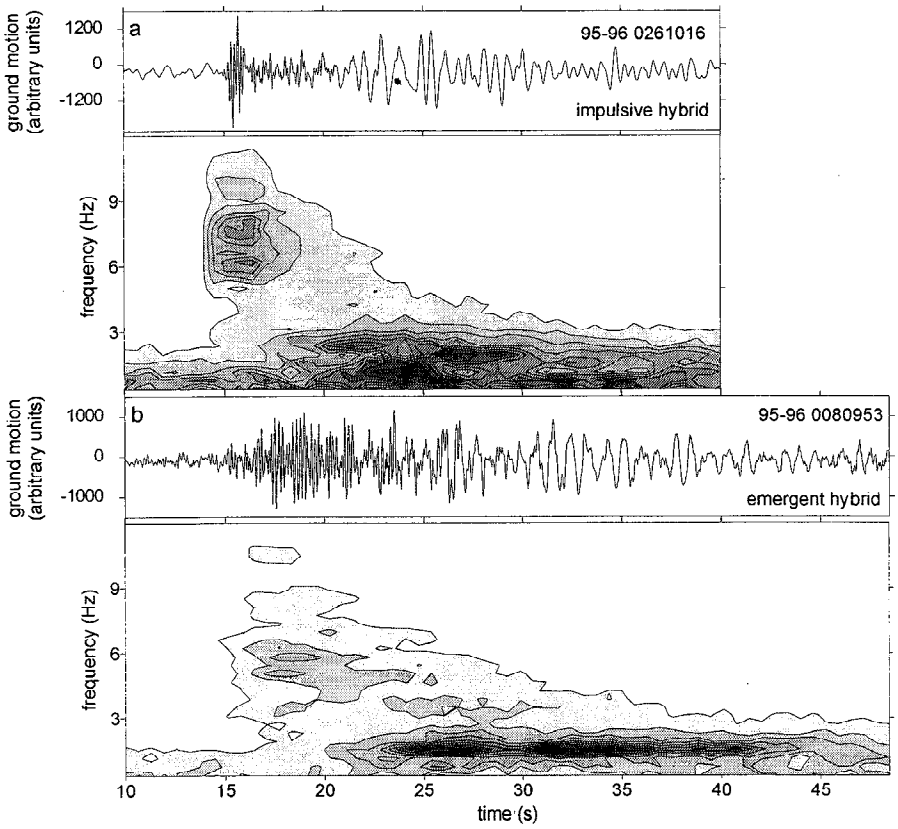

Figure 7. Examples of velocity seismograms and array-averaged spectrograms for (a) impulsive hybrid and (b) emergent hybrid.

show duration longer than 30 s; LP2 events have the smallest duration (around 10 s). LP1 and LP2 occur in seismic swarms while LP3 events are isolated in time. It can be observed that LP1 and LP2 seismic swarms presented a high number of events per hour in the continuous recording monitor (in some cases more than 100 per hour). Sometimes, this high occurrence rate makes difficult to distinguish between long-period events and volcanic tremor.

4.2.2. Hybrid events. These signals are characterized by an initial high-frequency phase, with a short duration (less than 5 s) followed by a monochromatic signal identical to that of the long-period events (Figure 7). The spectral content of the first phase is broad, from 1 to 12 Hz. The first phase is sometimes characterized by an impulsive, rich of high-frequency and short-duration first onset (impulsive hybrids), and sometimes by a more emergent first onset and longer duration, so-called emergent hybrids (Figure 7). The impulsive hybrids normally take place isolated in time, while the emergent hybrids occur clustered in time. The spectra for both types of hybrid show two predominant frequency bands, 1-3 and 4-8 Hz. The total duration of these events ranges between 30 and 60 s.

4.3. Volcanic Tremor

The presence of volcanic tremor in Deception Island can be clearly recognized on the monitor of the continuous recording station. Because of the limitation of the trigger system of the array, we could only record a maximum of 150 s of signal. During intense tremor episodes, several records 150 s long, which triggered the array recording system, permitted us to sample the evolution of the activity. We observed three kinds of volcanic tremors according to their spectral features (Figure 8). The first kind of tremor (the low-frequency tremor) is a low-frequency signal with a spectral peak between 1 and 2 Hz. The second kind of tremor (the spasmodic tremor) shows a very rough envelope, and a broader spectral content, with at least two predominant frequency bands, one between 2 and 3 Hz and the other between 4 and 8 Hz, the same bands observed for hybrids. The last kind of volcanic tremor (the quasi-monochromatic tremor) is characterized by a quasi-monochromatic high-energy signal peaked around 3 Hz, with the sporadic presence of secondary peaks (Figure 8). The occurrence of this type of tremor was not so frequent in the three surveys, as that for LP3 events.

4.4. Ice Quakes

Because of the presence of glaciers in Deception Island we recorded seismic events, produced by glacier ruptures, classified as ice quake events. We have recognized the ice-quakes in the data set by comparing them with the signals recorded in Livingston Island (Figure 1), where a seismic array with the same characteristics as that used in the present work was deployed [*Ibáñez et al.*, 1997b]. The ice quakes are characterized by a short duration, less than 10 s, and high-frequency content (up to 20 Hz). Visually, we observed a very high attenuation of the signal across the array and a slow apparent velocity. We believe that a few events of this kind could be included in our data set due to an error in classification, but this contamination should be small, affecting the data set in an insignificant way.

5. Properties of Event Clusters

The main part of the seismovolcanic activity recorded at Deception Island occurred as seismic swarms. In this section we

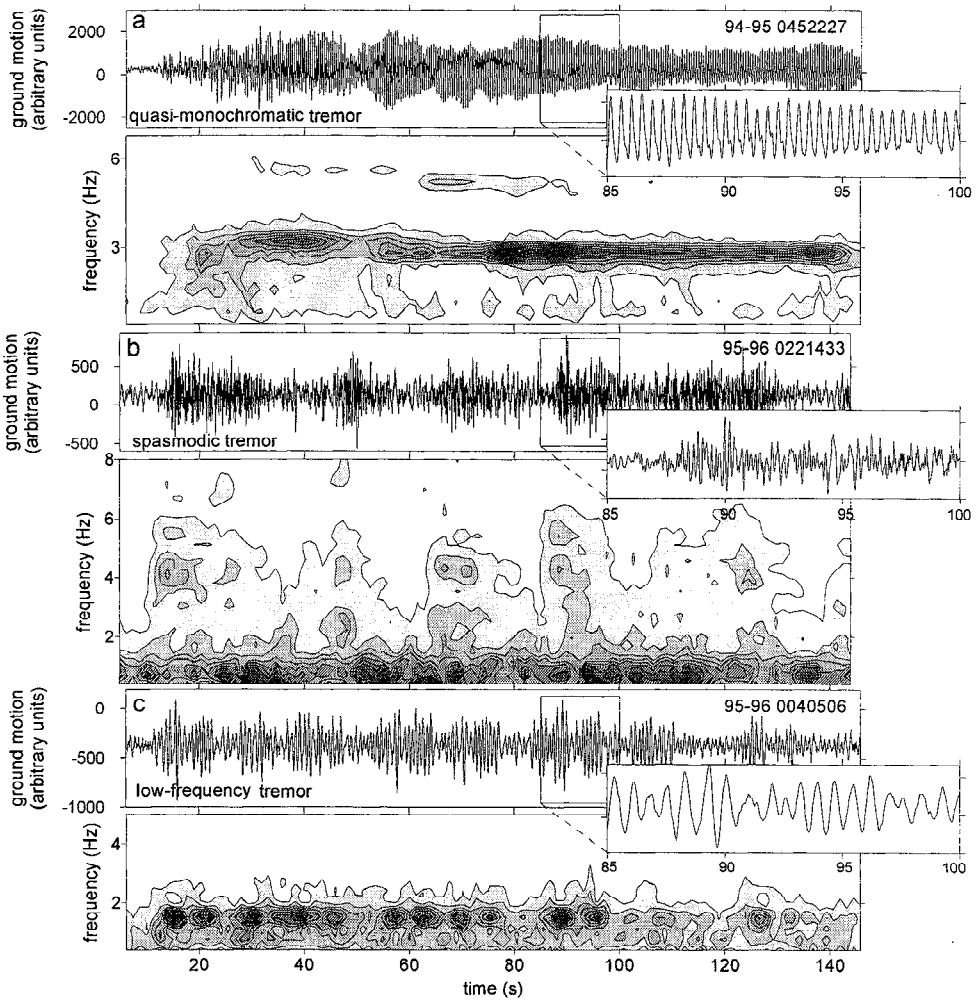

Figure 8. Examples of velocity seismograms and array-averaged spectrograms for (a) quasi-monochromatic tremor, (b) spasmodic tremor, and (c) low-frequency tremor.

describe the properties of three typical clusters, one of them composed basically of LP1 events and low-frequency tremor, the second one of hybrids and spasmodic tremors, and the last one of single pure long-period events. We have considered as seismic swarms those clusters of seismicity in which the daily number of events was greater than 30. The most important characteristic of the seismic activity of each cluster is the homogeneity of event type and spectral shape. The seismic activity recorded during the 1996-1997 survey was so weak that we cannot identify any clear cluster of events.

5.1. LP1 Events and Low-Frequency Tremor

The first type of seismic swarm is composed of LP1 events occurring so frequently that they form an episode of low-frequency tremor (Figure 9a). During experiment 5, swarms of this type were recorded (see Figure 4). The spectrograms calculated along the tremor episode show a stable spectral shape picked at a 1-3 Hz frequency band (Figure 9b). In the same figure we show three examples of array-averaged spectra calculated at three different time intervals during the same episode (Figure 9c). The only difference between them is the amplitude, while the main peaks remain stable in frequency and in bandwidth.

5.2. Emergent Hybrids and Spasmodic Tremor

The spasmodic tremor has a broader frequency content in comparison to the low-frequency tremor (Figure 10a). Often, this tremor appears as a sequence of isolated emergent hybrid events. We recorded three episodes of this type during the experiments (see Figure 4). This tremor is characterized by at least two predominant frequency bands, one at low-frequency (1-3 Hz) and the other at frequencies between 4 and 8 Hz. The array-averaged spectra, evaluated at three different time periods (separated by one day), once again show stability of the predominant frequency band (Figure 10).

5.3. Long-Period Seismic Swarm

This type of swarm is characterized by the clustering of both LP1 and LP2 events. This kind of clustering has the highest number of events per day, reaching up to 150 triggered events per day, and more than 100 events per hour for the February 5-9, 1996, swarm. Five episodes of this kind were recorded during the surveys. The spectral peak for LP1 and LP2 events is almost constant during the whole swarm.

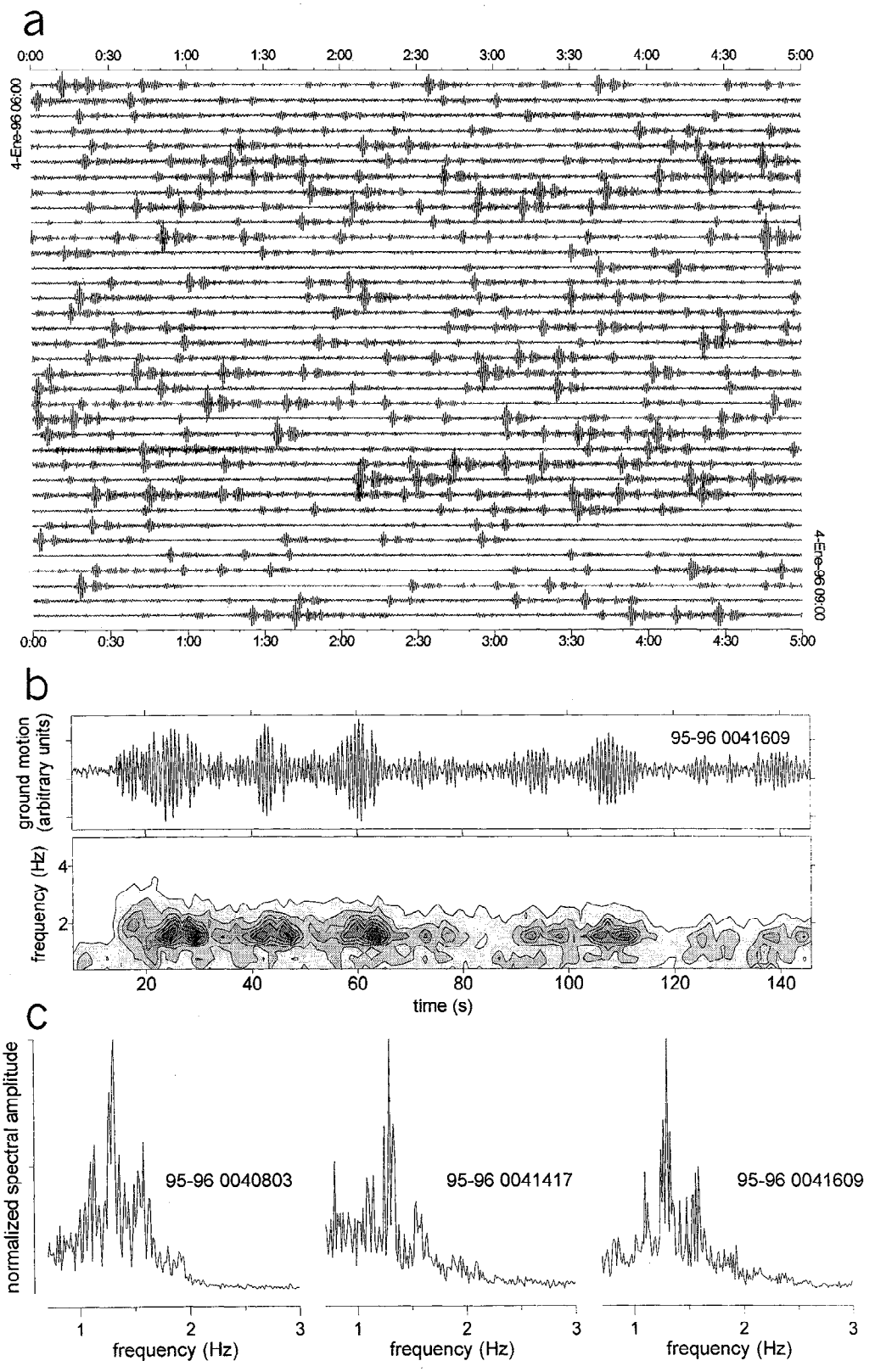

Figure 9. Example of an LP1 and low-frequency tremor episode. (a) Three hours of continuous recording. (b) Example of a 150-s-long velocity seismogram and array-averaged spectrogram of a low-frequency tremor. (c) Three array-averaged spectra of tremor samples showing the stability of the spectral peaks.

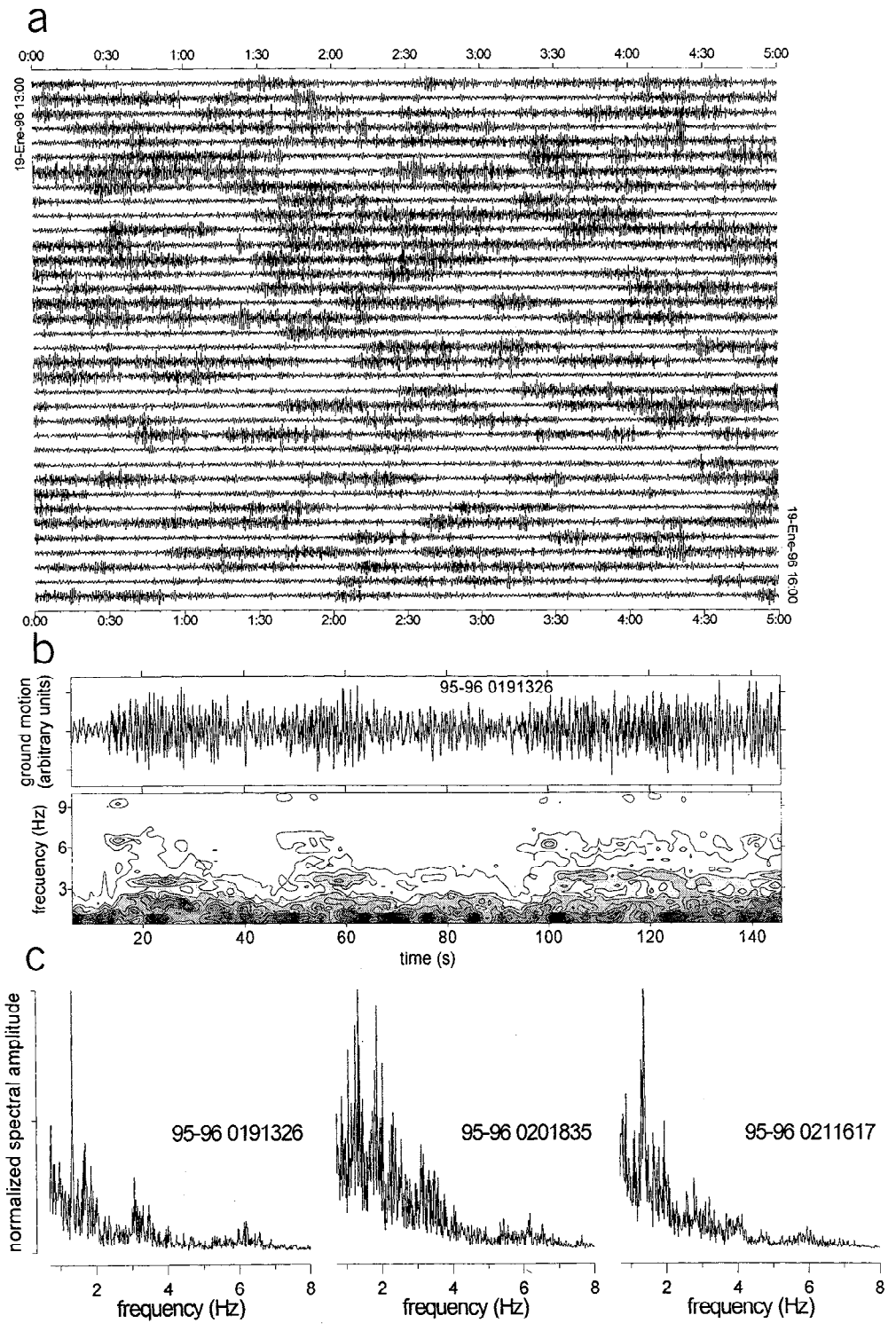

Figure 10. Example of a hybrid and spasmodic tremor episode. (a) Three hours of continuous recording. (b) Example of a 150-s-long velocity seismogram and array-averaged spectrogram of spasmodic tremor. (c) Three array-averaged spectra of tremor samples showing the stability of the spectral peaks. The time interval between samples is around 1 day.

6. Array Analysis: Source Location and Extent

6.1. Array Method

In this work we used the so-called zero lag cross-correlation (hereinafter referred to as ZLCC) technique [*Frankel et al.*, 1991] to measure the slowness and back azimuth of the whole recorded signals from the preevent seismic noise until the end of the wave packet for successive time windows. A detailed discussion of methodology and error estimation for this technique is described by *Del Pezzo et al.* [1997]. *Almendros et al.* [1999] introduced the circular wave-front approximation to this technique in order

to estimate the epicentral distance for seismic sources close to the array. The method used works in the time domain and has the following advantages, over the array techniques based on the Fourier analysis: it permits us to track the evolution of the source when the signal duration is short and the results are less sensitive to the window duration. [*Almendros et al.*, 1999]. However, this method needs more computer time than other methods and is not selective to multiple sources.

The cross-correlation function is defined by

$$R_{jk}(\tau) = \langle A_j(t)\ A_k(t+\tau)\rangle, \quad (1)$$

where $A_j(t)$ is the seismogram at the station j, and angle brackets indicate the time average. If τ_{jk} is the time delay between stations j and k, then R_{jk} will reach a maximum when the traces are shifted by τ_{jk}. If we calculate the normalized average of R_{jk}, R, over all the possible pairs of stations

$$R = \frac{1}{N^2}\sum_{j,k=1}^{N}\frac{R_{jk}(\tau_{jk})}{\sqrt{R_{jj}(0)R_{kk}(0)}}, \quad (2)$$

then this function R will take the maximum value when all the trace couples are shifted by τ_{jk}. Values of τ_{jk} can be expressed as a function of the apparent slowness vector components (S_x, S_y) in Cartesian coordinates. In the case of a planar wave front incoming to the array,

$$\tau_{jk} = |S|\left[(x_j - x_k)\sin\Phi + (y_j - y_k)\cos\Phi\right], \quad (3)$$

where

$$|S| = \sqrt{S_x^2 + S_y^2}, \quad (4)$$

and Φ is the back-azimuth epicenter-seismic array, given by

$$\mathrm{tg}\,\Phi = \frac{S_x}{S_y}, \quad (5)$$

In the case of a circular wave-front incoming to the array

$$\tau_{jk} = |S|\left[\sqrt{(x_k - D\sin\Phi)^2 + (y_k - D\cos\Phi)^2} - \sqrt{(x_j - D\sin\Phi)^2 + (y_j - D\cos\Phi)^2}\right], \quad (6)$$

where D is the epicentral distance. The problem of finding the $\boldsymbol{S}$ vector, which best fits the experimental data, is solved using a grid search in the parameter space. The slowness components (S_x, S_y) are allowed to range over an interval where we are sure that the solutions lie, using a grid step ($^{\Delta}S_x$, $^{\Delta}S_y$). For each step, a set of τ_{jk} is evaluated, and the quantity R is calculated. In the case of circular wave fronts the grid is threedimensional (S_x,S_y,D). The maximum averaged cross correlation (MACC) leads to the best estimate of the solution vector.

We used the following procedure to analyze the data: First, we selected the most energetic frequency band after a visual inspection of the spectra. For each frequency band we filtered the seismograms using a zero phase shift, four poles, and a Butterworth bandpass filter. LP events, monochromatic tremors, and volcano-tectonic earthquakes were filtered in a unique band, centered at the main spectral peak, while spasmodic tremors and hybrids were filtered in two bands centered around the two main frequency peaks. We used a moving time window with a duration that depended on the frequency band used in the filtering process. This window was selected in order to contain approximately two periods of the signal in each window. The time window is shifted each step with an overlap of 50%, and the ZLCC technique was applied each time step, initially in the planar wave front approximation. For VT earthquakes the analysis was restricted to only the first P-wave impulse, while for the other volcanic signals, the method was applied to the whole seismogram in order to put in evidence possible persistent sources, as already observed in other volcanic areas. We did not analyze ice quakes with this technique because of their lack of coherence across the array, due to their high dominant frequency and low propagation velocity. As the ZLCC technique is based on a grid search on all the possible values of the apparent slowness vector, we restricted the grid search to a range of values depending on the frequency band. By using information derived from a preliminary analysis of the apparent slowness, we selected the grid maximum and grid spacing of 4 and 0.08 s/km, respectively, for the frequency bands below 3.5 Hz and 1 and 0.02 s/km for higher frequency bands. In Table 1 we report the parameters used in the array analysis.

Table 1. Parameters Used in the ZLCC Procedure

Frequency Band (Hz)	Length (samples)	Duration (s)	S_{max} (s/km)	ΔS (s/km)
1.0-2.0	300	1.5	4	0.08
1.0-2.5; 1.0-3.5	200	1	4	0.08
2.0-3.5	160	0.8	4	0.08
3.0-6.0	100	0.5	1	0.02
4.0-8.0; 6.0-10.0	80	0.4	1	0.02

S_{max} is the grid size; ΔS is the grid search step.

6.2. Local Earthquake Source Location

Twenty earthquakes with S-P time ranging from 1.3 to 3.0 s were analyzed to estimate the hypocentral location. First, the array parameters (apparent slowness and back azimuth) were estimated applying the ZLCC array analysis to the first P-wave pulse. We analyzed these earthquakes in the 4-8 Hz frequency band, corresponding to the maximum spectral power, in order to avoid any possible influence from background volcanic signal or other noise source. After that, we back traced the ray through the velocity models reported in Table 2 and used the S-P time to fix depth and epicentral distance. In Table 3 we report array parameter, distance, and focal depth for each earthquake. The epicentral map, in which the focal depth is marked, is plotted in Figure 11. These 20 earthquakes have been located inside the Deception volcano area at a depth shallower than 1 km. We consider them to be the brittle response of the medium to the volcanic processes of the island, and for this reason, we classified

Table 2. Velocity Structure for Deception Island

Z (km)	Vp (km/s)	Vp/Vs
0.02	0.5	1.43
0.57	1.5	1.60
1.41	1.8	1.65
6.0	4.5	1.73
12.0	6.0	1.73
∞	8.0	1.73

Z, depth of every soil shell. Vp, P-wave velocity. Vs, S-wave velocity.

Table 3. Location of the Volcano-Tectonic Earthquakes

Number	Survey	Name	Back-azimuth (°N)	Apparent slowness (s/km)	S-P time (s)	Distance (km)	Depth (km)	MACC
1	95-96	0430423	28	0.39	1.6	2	1.0	0.65
2	95-96	0461637	284	0.38	2.1	2.5	1.0	0.64
3	95-96	0470147	351	0.24	1.3	1	1.0	0.71
4	96-97	3450641	188	0.29	1.5	1.3	1	0.57
5	96-97	3521638	187	0.35	1.5	1.7	1	0.54
6	96-97	3522106	184	0.31	3.0	2.9	1	0.59
7	96-97	3530010	184	0.28	2.6	2.3	1	0.54
8	96-97	3582037	188	0.35	1.8	2.0	1	0.75
9	96-97	0010423	178	0.33	1.3	1.4	1	0.87
10	96-97	0010429	178	0.35	2.4	2.6	1	0.83
11	96-97	0010714	169	0.23	1.7	1.2	1	0.70
12	96-97	0092112	309	0.13	1.7	4.6	7	0.67
13	96-97	0092120	297	0.16	1.7	5.4	6	0.79
14	96-97	0111920	172	0.28	1.7	1.5	1	0.72
15	96-97	0260142	192	0.30	2.2	2.1	1	0.77
16	96-97	0281222	178	0.29	1.7	1.6	1	0.61
17	96-97	0341603	47	0.18	1.6	4.1	4	0.96
18	96-97	0350549a	183	0.34	1.8	2.0	1.0	0.73
19	96-97	0350549b	180	0.28	1.4	1.2	1.0	0.79
20	96-97	0461421	7	0.16	2.7	11	8.0	0.89

them as volcano tectonic (VT) earthquakes. It is noteworthy to observe (Figure 11) the evident spatial clustering of VT earthquakes, aligned in the north-south direction, suggesting the presence of an active shallow fracture system near the array site.

6.3. LP, Hybrid, and Tremor Source Location

The ZLCC analysis applied to LP events shows (1) an almost constant MACC value (Figure 12) along the signals, between 0.5 and 0.7 (the maximum possible value is 1). (2) In many cases the preevent noise is correlated, with the same apparent slowness and back azimuth as the seismic events but with smaller MACC value. (3) For LP1 events a regular variation of the apparent slowness along the signal is observed. The apparent slowness value has an initial slow increase, from 1 to 2 s/km, and then it returns to 1 s/km (Figure 12). (4)) The average apparent slowness for LP1 and LP2 types is 1.5 s/km and of 0.3 s/km for LP3 events (Figure 13). (5) A stable back azimuth, independent of the spectral content for LP1, LP2, and LP3, centered around 200°N (Figure 13).

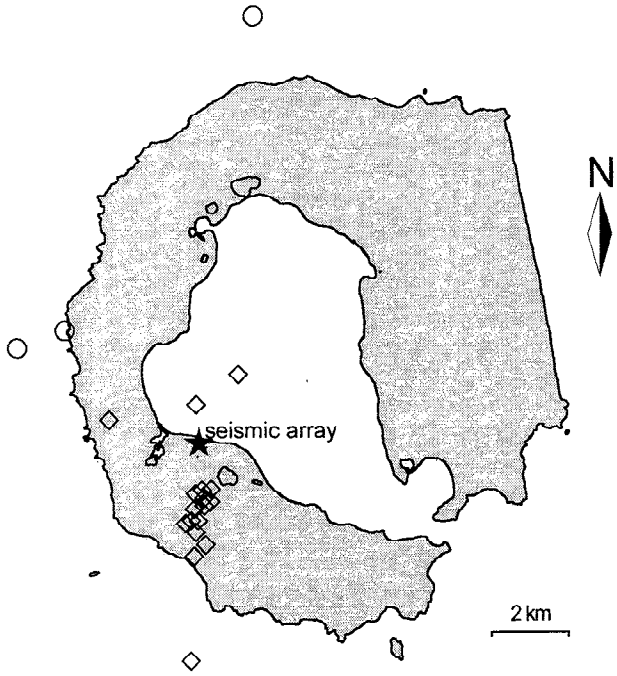

Figure 11. Epicentral map for the volcano-tectonic earthquakes reported in Table 3, plotted with different symbols according to the focal depth. Diamonds represent earthquakes with focal depth shallower than 5 km. Circles are earthquakes with focal depth between 5 and 15 km.

For hybrid events the ZLCC analysis was applied after bandpass filtering of 1-2 and 4-8 Hz (Table 1). The results (Figures 14 and 15) show (1) in the low-frequency band the pattern of MACC value, back azimuth, and apparent slowness is the same as that described for LP1 and LP2 events. (2) At high-frequency the highest MACC values are close to 1; the time duration of the well-correlated phases is short (mostly less than 2 s) although well-correlated signals for intervals as long as 5 s were also observed, as shown in Figure 14. (3) The apparent slowness of the high-frequency signals is lower than 0.5 s/km and in some cases lower than 0.2 s/km. The corresponding low-frequency phase, which follows the high-frequency arrivals, shows apparent slowness higher than 1 s/km. (4) In the majority of the solutions, there is a discrepancy between the back-azimuth solution for the high-frequency and the low-frequency phases, as reported in Figure 15.

The same analysis was applied to the quasi-monochromatic volcanic tremor showing the following features (Figure 16a) (1) the tremor starts with a phase with a low apparent slowness (around 0.2 s/km) similar to that observed for hybrids. (2) During the monochromatic sustained phase of the tremor the MACC values are low (between 0.4 and 0.5), indicating a low correlation of the waveforms among the array stations, with an apparent slowness of around 2 s/km but in some cases close to 4 s/km. (3) The average observed back-azimuth direction is around 180°, similar to that observed for LP events (Figure 17).

The low-frequency tremor (Figure 16b) shows the same results observed in the analysis of the LP1 and LP2 events, with very high MACC values, close to 0.9. Observing the Figure, we point

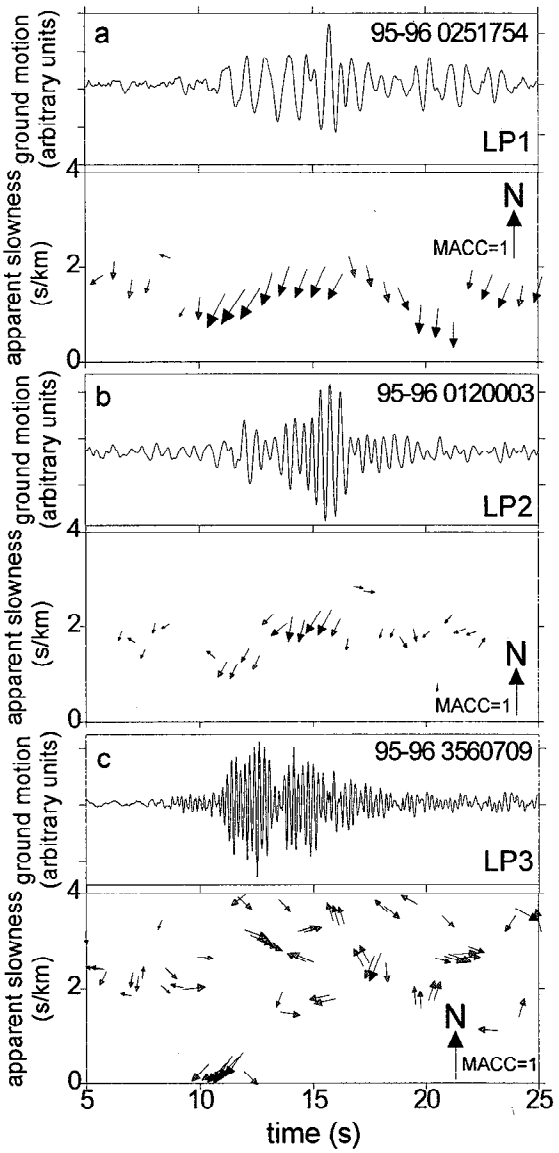

Figure 12. Examples of the solutions obtained using the zero lag cross correlation (ZLCC) method in the planar wave-front approximation for long-period events. (a) LP1 events, (b) LP2 events, and (c) LP3 events. Arrow directions represent the back azimuth and arrow size the maximum average cross correlation (MACC) value. An arrow marking the north, with MACC value equal to 1, is plotted in every example.

out the striking regularity of the well-correlated solutions along the signal, indicating the presence of a sustained volcanic tremor source.

The analysis of the spasmodic tremor has been performed again in both frequency bands, high and low. The main characteristic of the solutions, in both frequency bands, is the strong similarity with those obtained for the hybrids (Figure 16c). A similar result was obtained by *Almendros et al.* [1997], who analyzed a subset of the present data. It is noteworthy that solutions for the high- and low-frequency bands are different. At low-frequency, MACC values remain high and constant along the signal, similar to the patterns observed for the low-frequency-analyzed signals. At high-frequency, the high MACC values appear suddenly several times along the signal, coincident with the arrival of high-frequency wave packets and therefore with high-frequency burst in the spectrogram of the tremor. This observation indicates that the high-frequency signal source is discrete in time, while the source of the low-frequency signals seems to be sustained in time.

To obtain an estimation of the epicentral distance, we applied the circular wavefront approximation (relationship 6) to a subset of data. A portion of all the different event groups that contain low-frequency phases composes this subset; it was selected from the best signal-to-noise ratio. Array solutions of these events show a high apparent slowness, compatible with the hypothesis of surface waves incoming to the array. Results show that the main part of the selected events is located close to the array site, between 500 and 2000 m. Figure 18a plots the epicentral distribution for LP1 and LP2 events, showing that LP2 events have a seismic source closer to the array than LP1. In Figure 18b we plot the solutions for LP events, hybrids, and tremors. It is clearly observable that there are two spatial clusters of solutions, the first coincident with the LP2 source area and the second located at a larger distance. It is noteworthy that volcano-tectonic earthquakes and long-period events share a similar epicentral region, located toward the south and close to the array site. Volcano-tectonic earthquakes are located toward the southern border of the LP source area. Taking into account that the azimuth error derived from the ZLCC method is around 10°, VT and LP source locations are very similar.

7. Polarization Analysis

To perform this analysis, we used data recorded by the broadband sensor (Figure 2). We used this instrument because it has a flat response between 0.033 and 50 Hz and therefore we can apply our analysis over a broad frequency range.

7.1. Particle Motion

The E-W and N-S components were rotated in the horizontal plane into radial and transverse components, using the source-array direction obtained from the array analysis. Then, rotated seismograms were filtered at the same frequency bands used in the array analysis: LP and monochromatic tremor at low-frequency, hybrids and spasmodic tremor at both high and low frequencies (see Table 1). An example of the results obtained from this analysis is shown in Figures 19 and 20 for long-period, hybrid, and spasmodic tremor events. The particle motion pattern was studied in the same window length used for the ZLCC analysis, sliding in time along the highest-energy portion of the seismogram. Long-period events (LP1 and LP2) and the low-frequency tremor show a complex particle motion, without depicting any particular pattern that could be associated with the presence of body wave packets. The high-frequency phases of the hybrid events show a clear P-wave composition with no evidence of shear waves; the successive low-frequency phases show the same complex pattern observed for long-period events. The high-frequency wave packets composing the spasmodic tremor show an almost vertical particle motion pattern, compatible with compressional waves. The low-frequency phases of this kind of tremor show the same complex pattern observed for the low-frequency part of all the other events. The array analyses show that these waves (for LP events and tremor), due to their low apparent velocity at a low-frequency band, are compatible to surface waves. Contrary to other volcanic areas such as Etna [*Seidl and Hellweg*, 1991; *Bianco et al.*, 1996] or Stromboli [*Del Pezzo et al.*, 1992; *Chouet et al.*, 1997], where particle motion analysis indicated clearly the type of surface waves recorded, the

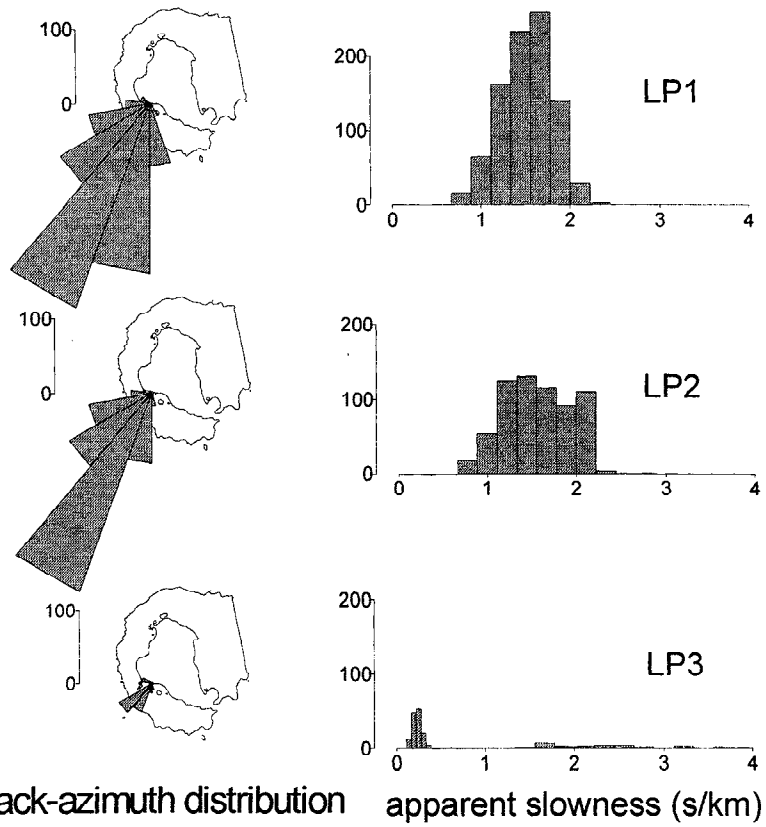

Figure 13. Back azimuth and apparent slowness histogram distribution obtained for long-period events. The center of the back-azimuth distribution is on the array site. The vertical scale represents the number of well-correlated solutions (MACC > 0.5).

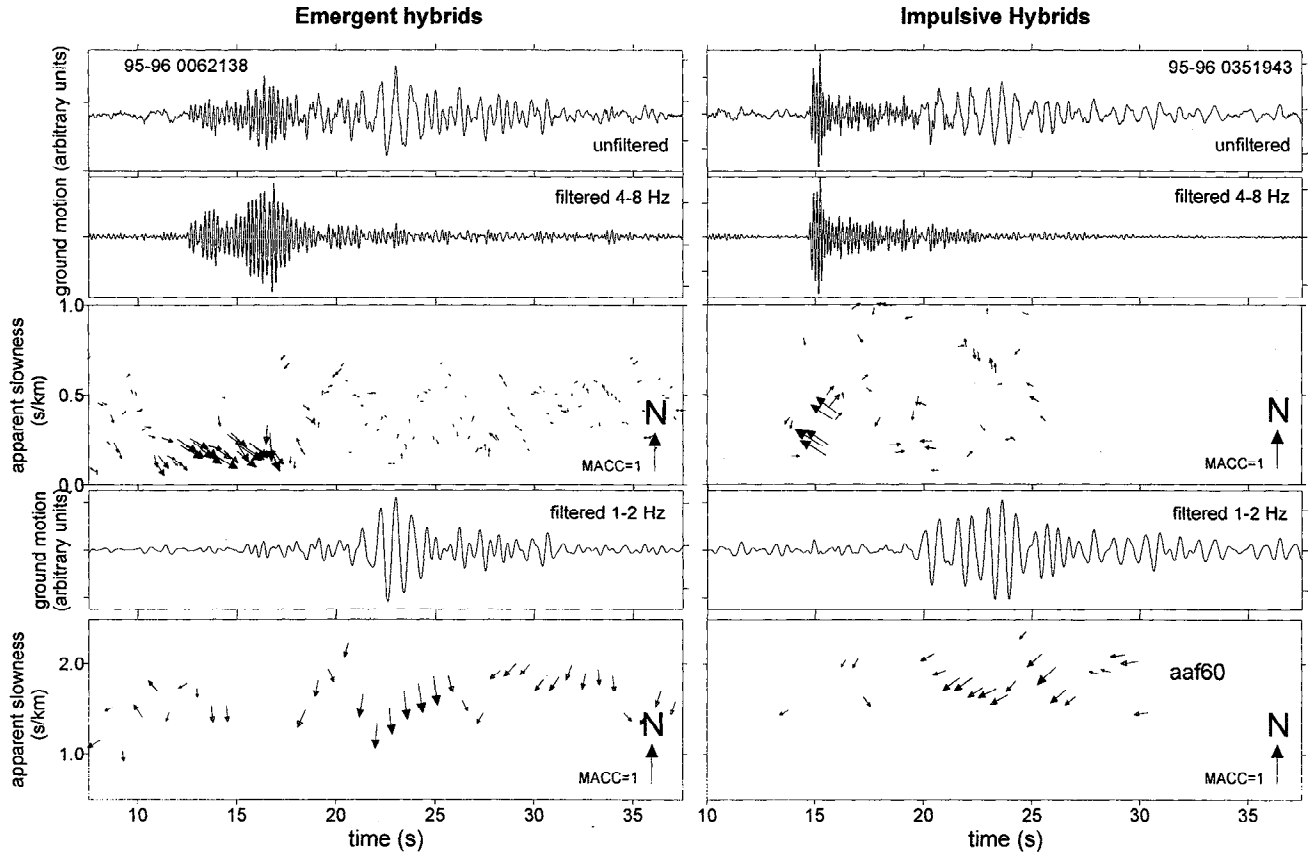

Figure 14. Same as Figure 12 for (a) emergent hybrid event and (b) impulsive hybrid event. This analysis was performed in the high- and low-frequency bands.

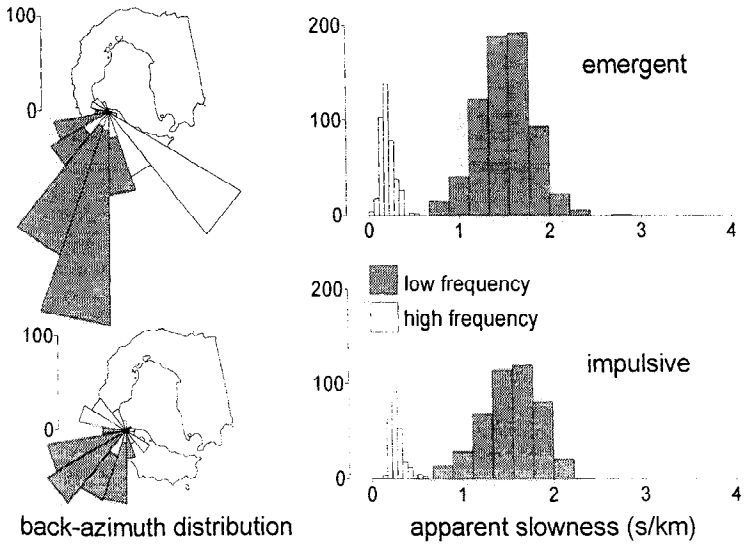

Figure 15. Same as Figure 13 for hybrid events. Low-frequency solutions are shaded, and high-frequency solutions are white.

results obtained for the low-frequency signals at Deception Island are very complex, and such a pattern is not observable. Therefore we cannot identify the type of surface waves we recorded.

7.2. Covariance Matrix

We applied a polarization analysis in the time domain, using the covariance matrix technique [*Kanasewich, 1981*], to a subset of data recorded by the broadband station, in order to quantify better and to check the particle motion analysis. In the Appendix we report a resume of this technique.

First of all, we tested the method on a well-recorded local earthquake (S-P=4.2 s) with clearly visible P and S waves. Results of this test are shown in Figure 21a, where the duration of pure P and S direct waves turn out to be not longer than 0.5 s. The application of the covariance matrix method to the low-frequency signals, for whatever type of event, confirms the observation done with the particle motion analysis: a complex surface wave pattern, with no clear wave polarization. On the contrary, the analysis of the high-frequency wave packets composing hybrids and tremor shows the presence of clear P-wave arrivals (Figure 21) and the absence of clear S waves. In several analyzed events the duration of the pure P waves are longer than a few seconds, with a maximum duration of 5 s (Figure 21c). In some cases a clear multiple arrival of pure P waves is visible along the signal (Figure 21b).

8. Energy Evaluation

In recent years it is common [e.g. *Gil Cruz and Chouet*, 1997] to report volcanic signal amplitudes in terms of a normalized displacement amplitude known as reduced displacement (D). This parameter is defined as the amplitude of the volcanic signal, corrected for the geometrical spreading and instrument response. In the case of surface waves the reduced displacement can be expressed as [*Aki et al.*, 1977; *Aki and Koyanagi*, 1981; *Fehler*, 1983]

$$D = U_{rms}\sqrt{\lambda r}\,, \tag{7}$$

where λ is the wavelength, r is the source-receiver distance, and U_{rms} is the rms of the ground displacement. For shallow sources the seismic moment rate for the volcanic tremor is given by [*Fehler*, 1983]

$$\dot{M}_0 = 6x10^{18} D\,, \tag{8}$$

There is a similar expression proposed by *Aki and Koyanagi* [1981] for body wave arrivals

$$D = U_{rms}\, R\,, \tag{9}$$

where R is the hypocentral distance. This relationship is useful in the study of deep sources for which body wave contribution is dominant.

We apply these formulas to the seismic events recorded in the 1995-96 survey to obtain an estimation of the energy involved in the source processes. This survey contains the greatest number of events and clusters of the three experiments. The polarization analysis has indicated that for the most part a mixing of different types of surface waves compose all the observed low-frequency wave trains. Therefore the relationships (7) and (8) were applied to the low-frequency component of the volcanic signals, i.e., the whole signal in the case of long-period events and tremor, and the low-frequency wave trains for hybrids and spasmodic tremor. The circular wave-front approximation has provided an estimation of the epicentral distance between source and array. In the present analysis we used the average distance of r = 1 km. In Figure 22a we report the individual and cumulative seismic moment for isolated volcanic events. As it can be observed, sudden steps are related to the occurrence of seismic swarms and not to single high-energy shocks. Because of the trigger mode recording of the seismic array we cannot estimate the real duration of the tremor episodes and therefore their seismic moment. If we compare only the seismic moment rate, proportional to the reduced displacement (Figure 22b), we obtain a very similar pattern for every type of event. The reduced displacement ranges from 1 to 9 cm^2, and the average value is close to 2 cm^2. The greatest reduced displacements are measured for events belonging to long-period seismic swarms. The uniformity of the reduced displacement values reveals the time

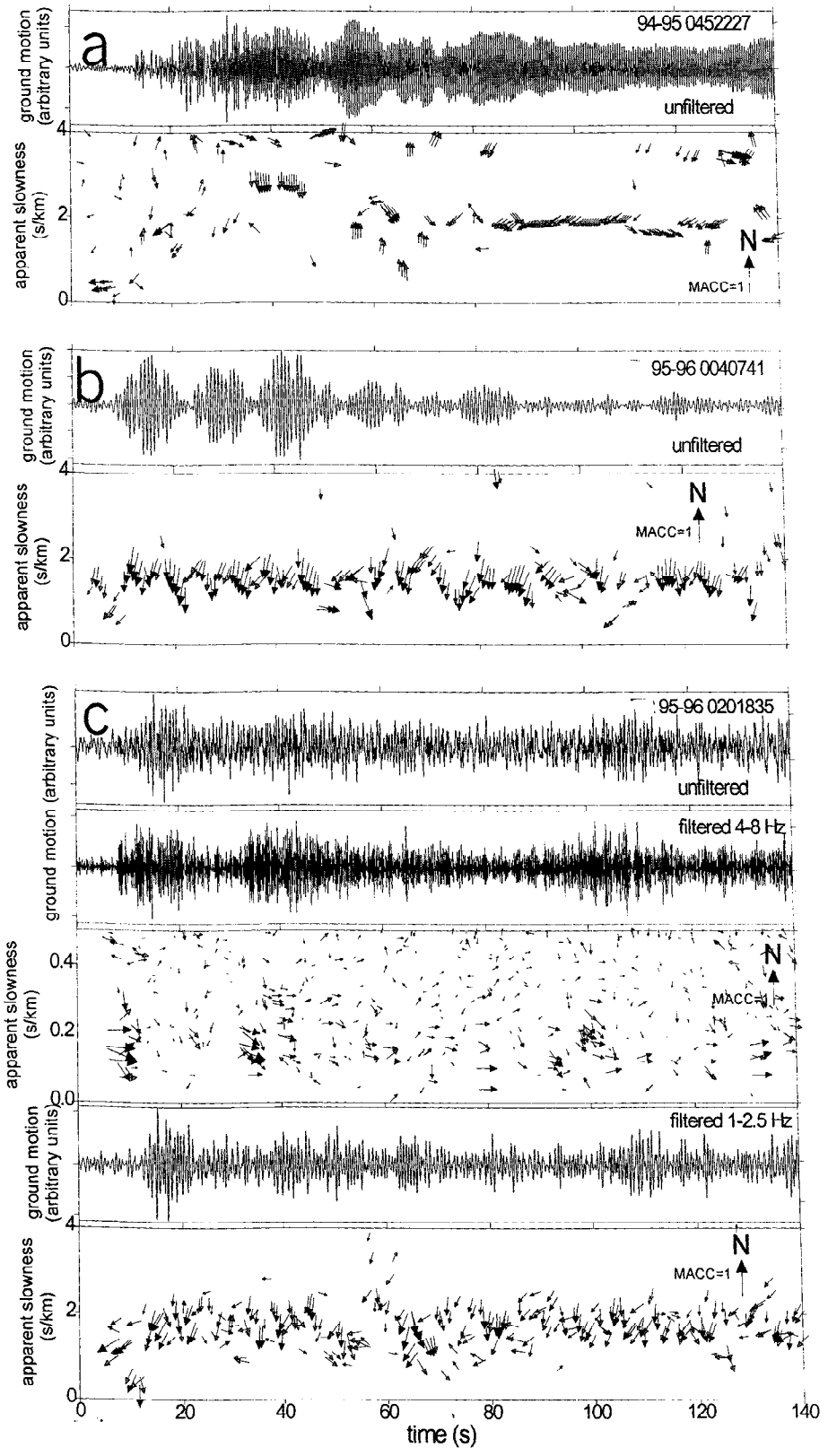

Figure 16. Same as Figure 12 for (a) quasi-monochromatic tremor, (b) low-frequency tremor, and (c) spasmodic tremor. This last kind of volcanic tremor was analyzed in the high- and low-frequency bands.

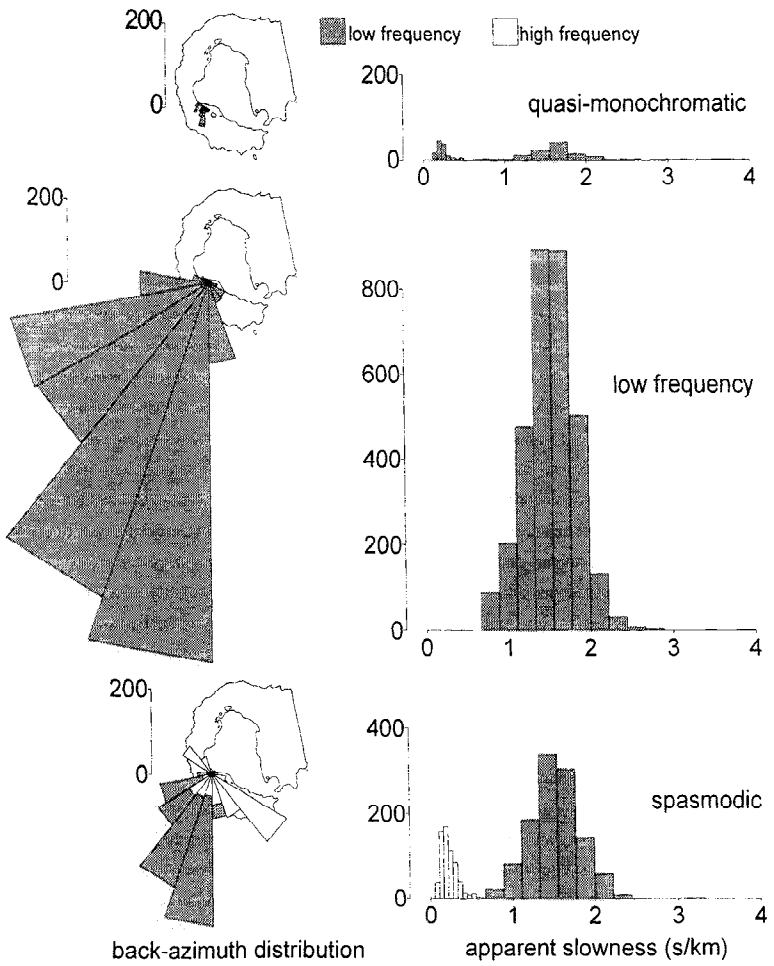

Figure 17. Same as Figure 13 for volcanic tremors. Low-frequency solutions are shaded, and high-frequency solutions are white.

stationarity in the source energy release, the source processes. There is an important relationship between the stationarity of these source processes, the invariance of the spectral properties and the stability of the hypocentral solutions.

For body waves we used relationship (9) with a distance of R = 1.5 km, assuming a depth of 1 km. We analyzed only the first high-frequency phase of the hybrid events. Figure 22c shows the reduced displacements for the hybrids indicating that impulsive hybrids have higher reduced displacement than the emergent ones. In any case, the average values are similar to those obtained at low-frequency.

9. Discussion

9.1. Summary of Experimental Evidences

The visual and spectral classification of the seismic events at Deception volcano shows the existence of long period and hybrid isolated seismic events and of low-frequency, quasi-monochromatic and spasmodic continuous tremors. All spectra have the highest amplitudes in the frequency band between 1 and 4 Hz, while hybrids and spasmodic tremors have also significant amplitudes in the high-frequency band (4 – 10 Hz).

There are two different types of spectral behavior in the low-frequency band. The most common corresponds to a series of nonregularly spaced peaks, while the second shows regularly spaced harmonics of a fundamental peak. In the first group we distinguish two subsets that are differentiated by the spectral band where the main peaks appear and can be associated with the spectra of LP1 and LP2. The spectral pattern at frequencies below 4 Hz for hybrids, low-frequency tremor, and spasmodic tremor can always be associated with one of them. The second group is represented by the LP3 spectra and incorporates also the quasi-monochromatic tremor.

The array analysis indicates that almost all the well-correlated low-frequency signals share similar array parameters (slowness and back azimuth). The average back azimuth is around 200°N, and the average slowness is around 1.5 s/km, with a gradual increase of the apparent slowness along the signals from 1 to 2 s/km. The ZLCC technique, applied with the hypothesis of a circular wave front incident to the array, gives an estimate of the source position for the low-frequency phases of hybrids and for the long-period events. Results show that all the seismic events have the same source area, close to the array site. At high-frequency the observed apparent slowness for well-correlated solutions is confined in the 0.2 - 0.5 s/km interval, and their back azimuth does not coincide with the back azimuth estimated for the low-frequency phases of the same event.

The polarization analysis shows that the first phase of hybrids and spasmodic tremors is mostly composed of P waves, followed

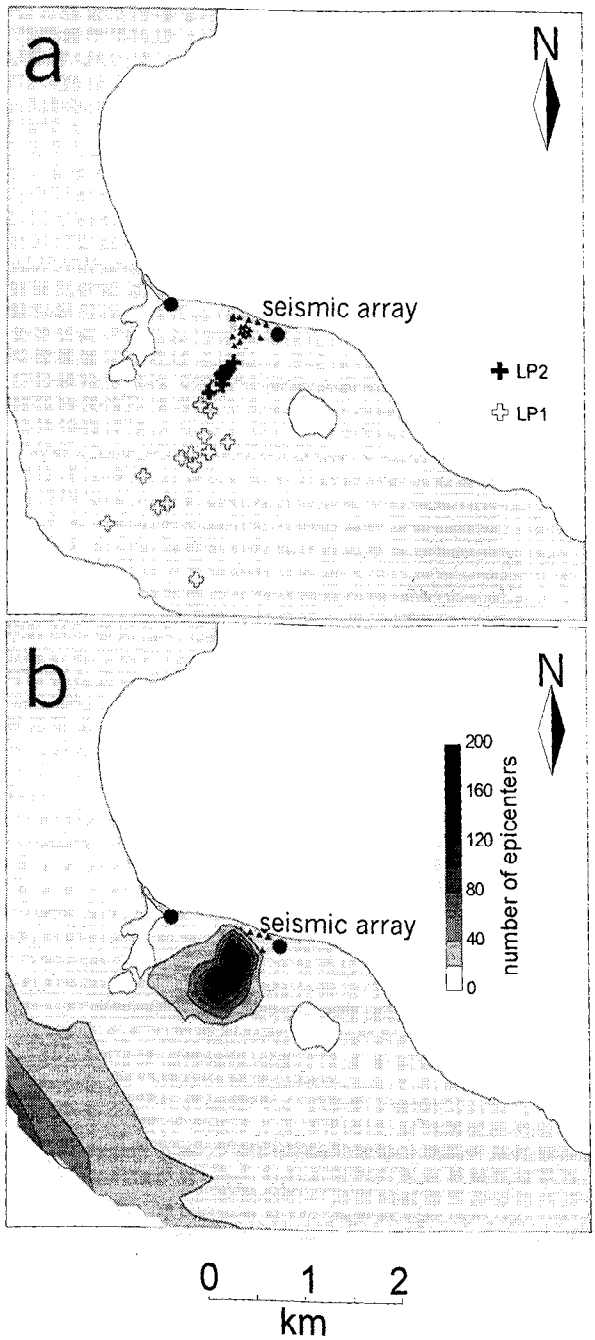

Figure 18. (a) Epicentral map of LP1 (gray) and LP2 (black) events belonging to a seismic swarm, obtained using the ZLCC method with the circular wave-front approximation. (b) Contour map of the number of epicenters for LP1 and LP2 events, hybrids, and low-frequency and spasmodic tremor obtained in the low-frequency band with the circular wave-front method.

by a second phase that can be interpreted as composed of surface waves. No clear shear waves are evidenced by the polarization analysis. Sometimes the high-frequency first phase of hybrids is composed of multiple P-wave phases. In the case of spasmodic tremors and hybrids, several high-frequency P-wave arrivals are observed to be distributed along the signal. Therefore the first phase comes to the array with a low apparent slowness, indicating that the high-frequency source is not located in the proximity of the surface. The corresponding low-frequency phase is shallow and close to the array. Since the existence of two sources separate in space and closely related in time is not reasonable, we prefer to hypothesize the existence of a unique source that produces both effects.

From the energy evaluation, we have found that the reduced displacement values for surface and body waves are confined to a narrow interval, suggesting that there is uniformity in time in the source processes, regardless of the type of seismovolcanic event.

VT seismicity is located close to the array at a depth shallower than 1 km and is distributed in a north-south direction. This activity shares the same epicentral region as the volcanic events and suggests the presence of an active shallow fracture system close to the same region where the other seismovolcanic signals are located.

From spectral, frequency slowness, and polarization analyses, we can deduce that spasmodic tremor is generated by the occurrence of dense swarms of hybrid events, while the low-frequency tremor is the superposition of dense swarms of long-period events. Single events and tremors share the same spectral properties, array solutions, and polarization properties that appear together during the seismic swarms. Several authors have made similar interpretations of the composition of the volcanic tremor on other volcanoes, including *Seidl and Hellweg* [1991] at Etna by polarization analysis, *Chouet* [1996] at Kilauea, and *Gil Cruz and Chouet* [1997] at Galeras volcano.

9.2. Conceptual Model of Seismovolcanic Source

The source model for the seismovolcanic signals at Deception Island should explain all the experimental evidences summarized above, taking into account the geological characteristics of the region which suggest the presence of a widely spread aquifer and the existence of hot materials close to the surface. To obtain this possible source model, first it is necessary to establish if the spectral characteristics observed are path or source effect. We recorded also very local earthquakes (VT seismicity). These earthquakes did not show any predominant peak in the 1-4 Hz frequency band. Therefore it seems to be clear to assume that the low-frequency contain observed in the spectra of the seismovolcanic signals is due to a source effect.

We can imagine two possible source models to explain the generation of the events belonging to the first spectral group (spectra with nonregularly spaced peaks). In the first model, a sudden phase change in the aquifer, coming in contact with hot rocks, produces a high-frequency wave train, while the low-frequency wave trains are generated by trapped surface waves in the layered shallow structure. In the second model, a sudden pressure step occurring at a depth in a fluid-filled crack put the crack itself in auto oscillation. We assume the presence of a crack due to the nonregularity of the low-frequency peaks. A two- or three-dimensional source model is necessary to explain these spectral characteristics. The high-frequency signal is produced at depth by the pressure step, and the low-frequency is produced by the crack auto oscillation.

In the first model, a deep explosive source, we cannot easily explain either the different back azimuth between high- and low-frequency coherent arrivals or the high amplitude of the low-frequency wave trains. Moreover, we would expect the presence of Rayleigh waves to be more energetic than those observed through the polarization analysis.

In the second model (Figure 23), the phase change occurs underneath the array site (as inferred by the low apparent slowness) and produces a resonance of a fluid-filled crack. The high-frequency waves are produced by the phase change occurring at any position along the lower edge of the crack. The

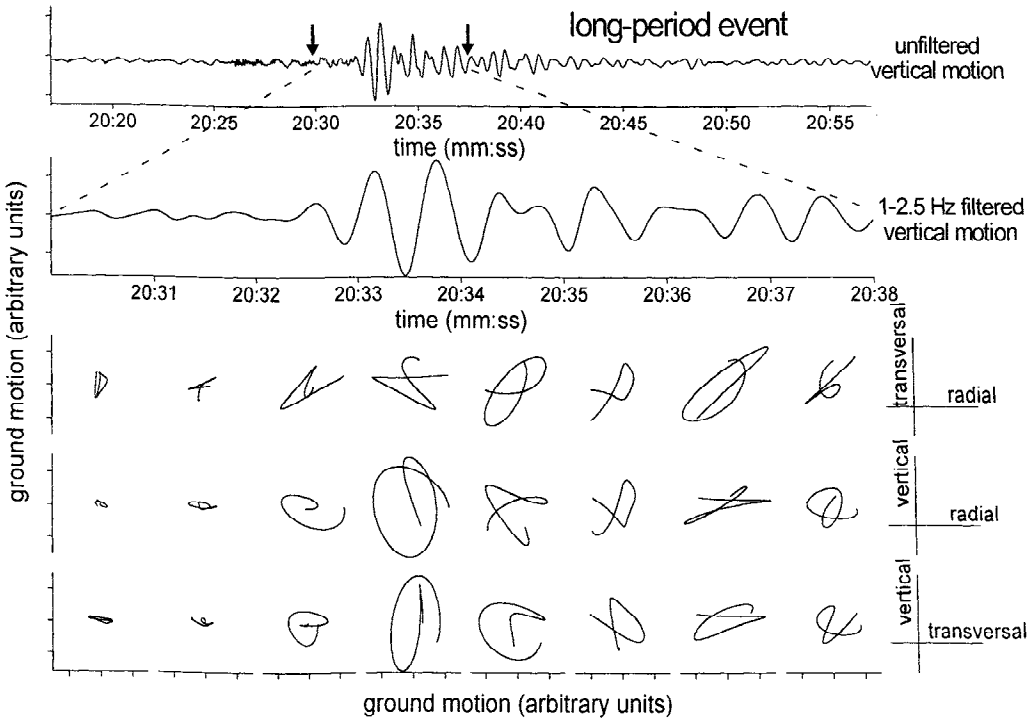

Figure 19. Particle motion plots for a long-period event using the broadband records. This study was performed along the most energetic portion of the seismogram, with the same window length used for the ZLCC analysis.

low-frequency waves are generated by the resonance of the whole crack and then will have approximately the same back azimuth for any event, depending on the spatial orientation of the crack. The differences between the back azimuth observed for low and high-frequency is thus a perspective effect due to the vicinity of an extended crack system. This hypothesis is confirmed observing Figure 23b. It shows the solutions in the apparent slowness plane for three hybrid events recorded on Deception Island. The back azimuths indicated by these solutions in high and low frequencies can be sketched by sources a, b, and c of Figure 23a. Only the arrivals from source b (body and surface waves) share the same back azimuth. However, both a and c show differences between the back azimuth of the body and the surface waves, due to the projection on the horizontal plane. The increasing trend of the apparent slowness observed in the low-frequency trains would be explained assuming that the crack resonance activation propagates toward the surface. The complex low-frequency wave pattern is due to the mixed contribution of P, SV, and SH waves radiated by the source (according to the model developed by *Chouet* [1986, 1988, 1992]) and to the generation of surface waves in the multiple-layered structure of the island, composed of frozen soil and different volcanic shells.

This conceptual model could provide a unique source mechanism for long period and hybrid events and for low-frequency and spasmodic tremors. The different spectra can be associated with different crack dimensions and properties. Assuming the model developed by *Chouet* [1992], the different energy of the initial high-frequency wave trains of the signals is explained by different risetime function of the pressure pulse, which triggers the oscillation of the fluid-filled crack. When the risetime is sharp, we observe the highest energy of the high-frequency waves. A smooth variation of the risetime function will change the high-frequency contribution to the spectrum, producing the different types of signals. When the pressure step appears isolated, the duration of this first phase is short. In the case of multiple activation of the source, we record first phases as long as 5 s. Pressure steps repeated for several minutes or hours produce the volcanic tremor. In the present source model, the seismic events that are classified as hybrids, based on their spectral properties, do not represent a fracture producing the crack opening, accompanied by its resonance (as described by *Lahr et al.* [1994], for Redoubt volcano). The so-called hybrid events at the Deception volcano share the same source mechanism as the long-period events. We have to point out that this conceptual model of single crack as shown in Figure 23 is an oversimplification and that reality may be a complex crack system with different sizes and orientations.

LP3 events and quasi-monochromatic tremor, due to their spectral properties, can be explained by a different mechanism, consisting of the resonance of an organ pipe conduit [*Chouet*, 1985; *Ferrazzini and Aki*, 1992]. In this case, the peaks of the spectra are overtones of the fundamental frequency (Figure 24). This spectral pattern reveals that in the source process a dimension of the source is dominant over the other two, and a pipe source model would be enough.

9.3. Quantification of Source Model

Three kinds of geometry have been investigated in theoretical studies of the resonance and elastic radiation from a fluid-filled body in a volcano. These are the fluid-filled sphere [*Crosson and Bame*, 1985], pipe [*Chouet*, 1985] and crack [*Aki et al.*, 1977; *Chouet*, 1986, 1988, 1992]. On the basis of the fact that the spectral peaks of the seismovolcanic activity of the LP1 and LP2 types are not equally spaced, we selected the rectangular crack model of *Chouet* [1992] to calculate the source dimensions and properties. For the LP3 type, where the spectral peaks are natural

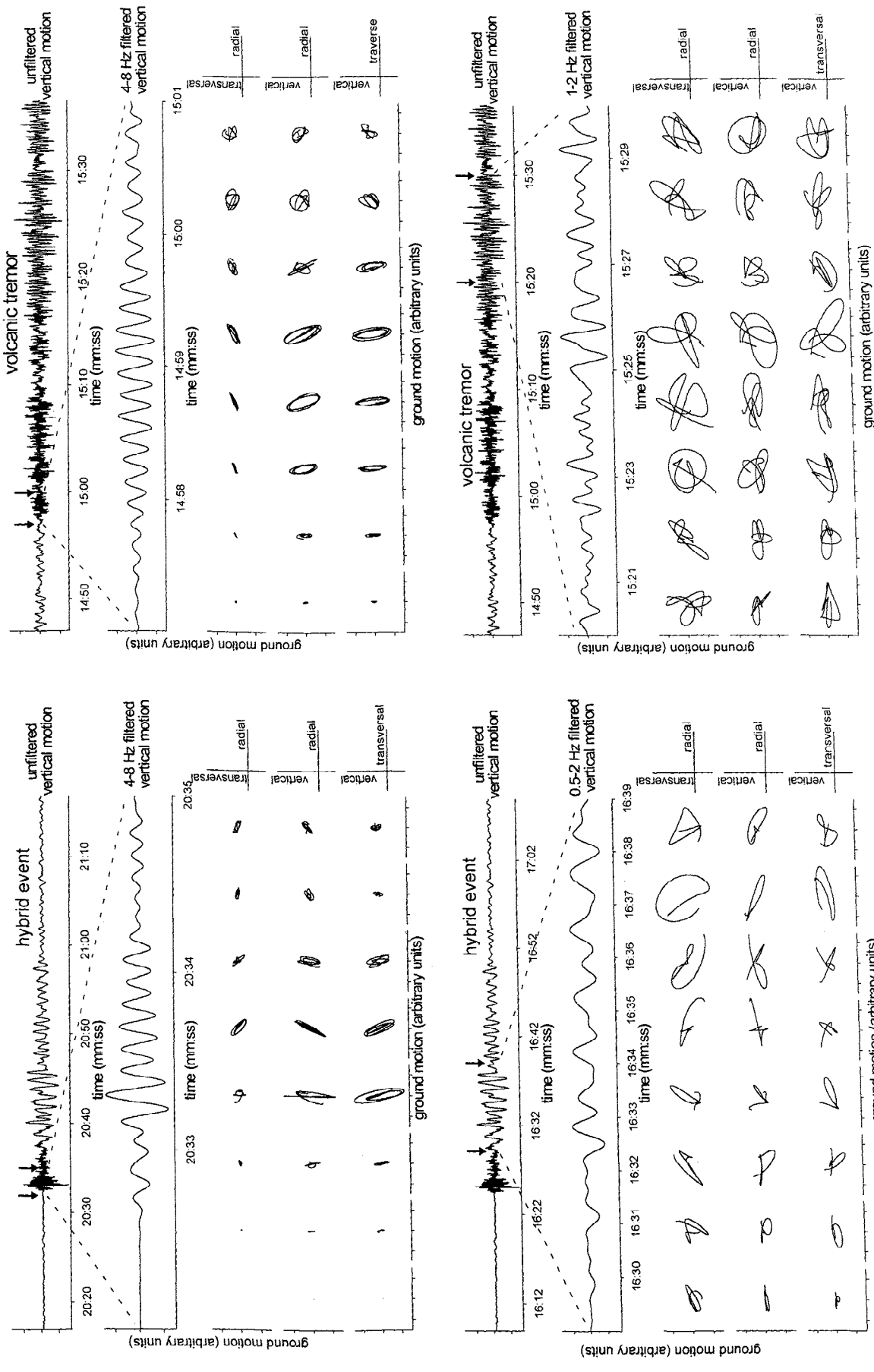

Figure 20. Particle motion plots for an impulsive hybrid and the beginning of a spasmodic tremor using the broadband records. The study was performed at low-frequency along the most energetic portion of the seismogram and at high-frequency during the first onset of the signal, with the same window lengths used for the ZLCC analysis.

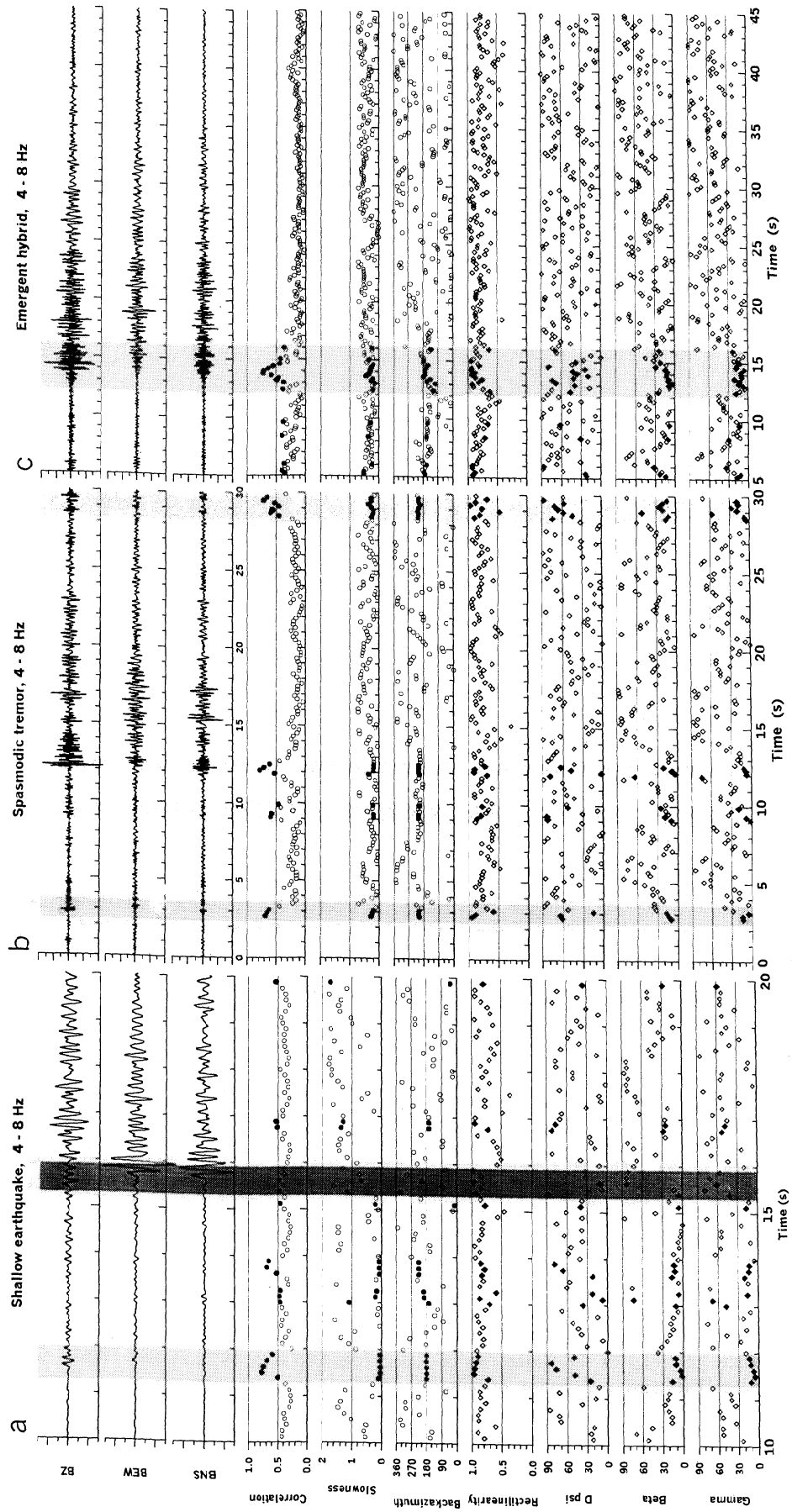

Figure 21. Examples of the results of the covariance matrix analysis for (a) a regional earthquake, (b) the beginning of a spasmodic tremor, and (c) a hybrid event in the high-frequency band. Solid dots are the well-correlated solutions. The arrival of P waves is identified by high correlation and low beta and gamma values. They are marked in the figure with vertical dashed lines.

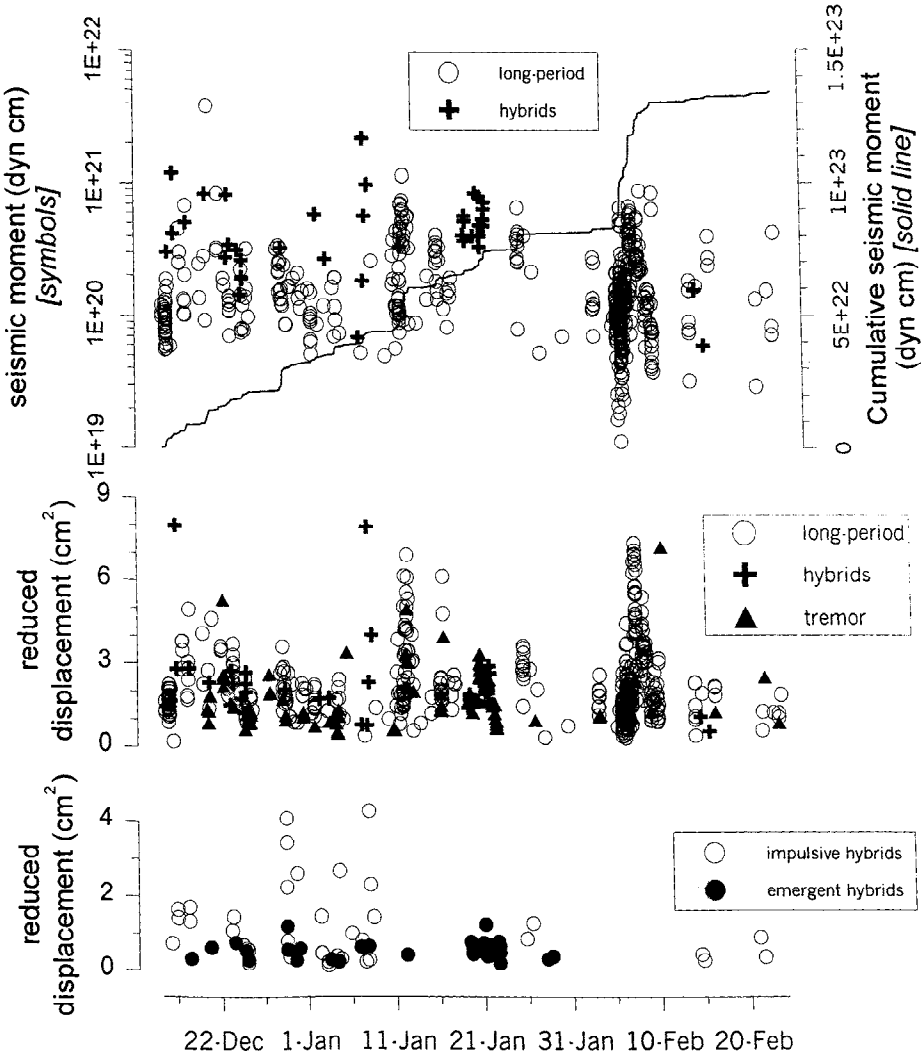

Figure 22. Time history of the reduced displacement and seismic moment of the events recorded during the 1995-96 survey. (top) Seismic moment obtained for the low-frequency phases of long- period and hybrid events. The solid curve is the accumulated seismic moment. (middle) Reduced displacement for the low-frequency phases of long period, hybrid, and tremor signals. (bottom) Reduced displacement for the high-frequency phases, considered as body waves, of impulsive and emergent hybrid events.

harmonics of a fundamental peak, we will consider the organ pipe model.

9.3.1. Fluid-Driven Crack Model. The fluid-driven crack model considers the resonance of a fluid-filled crack as the source for long-period volcanic activity [*Chouet*, 1986, 1988, 1992]. Using the finite difference method, *Chouet* [1986] obtained the response of a fluid-filled crack to an impulsive pressure transient by simultaneously solving the equations of elastodynamics in the solid and the equations for mass and momentum transfer in the fluid. The crack geometry and the physical properties of the fluid and solid fix the frequencies of the modes of the crack wave. The relative excitation of these modes depends on the position and characteristics of the pressure transient, and the boundary conditions for fluid flow at the crack perimeter. In Chouet's analysis the crack aperture is much smaller than the seismic wavelengths of interest, and the fluid dynamics in the fracture are treated as being two-dimensional. *Chouet* [1986] found that the resonant periods of the fluid-filled crack are much longer than those expected from acoustic resonance because of the presence of a slow wave, which he called the crack wave. This wave is always slower than the acoustic speed of the fluid and inversely dispersive, showing a strong decrease in wave speed with increasing wavelengths. *Chouet* [1986, 1992] has investigated the dispersion characteristics of the crack wave. The relationship between the phase velocity of the crack wave V and the dimensionless wavelength $\Lambda_L=\Lambda/L=2/n$ $(n = 2, 3, ...)$ (where L is cracklength) is a decreasing curve parameterized by the crack stiffness (C), an important parameter controlling the speed of the crack wave, and defined as [*Aki et al.*, 1977; *Chouet*, 1986]

$$C = \frac{b}{\mu}\frac{L}{d}, \tag{10}$$

where b is the bulk modulus of the fluid, μ is the rigidity of the solid, and L and d are the crack length and aperture, respectively.

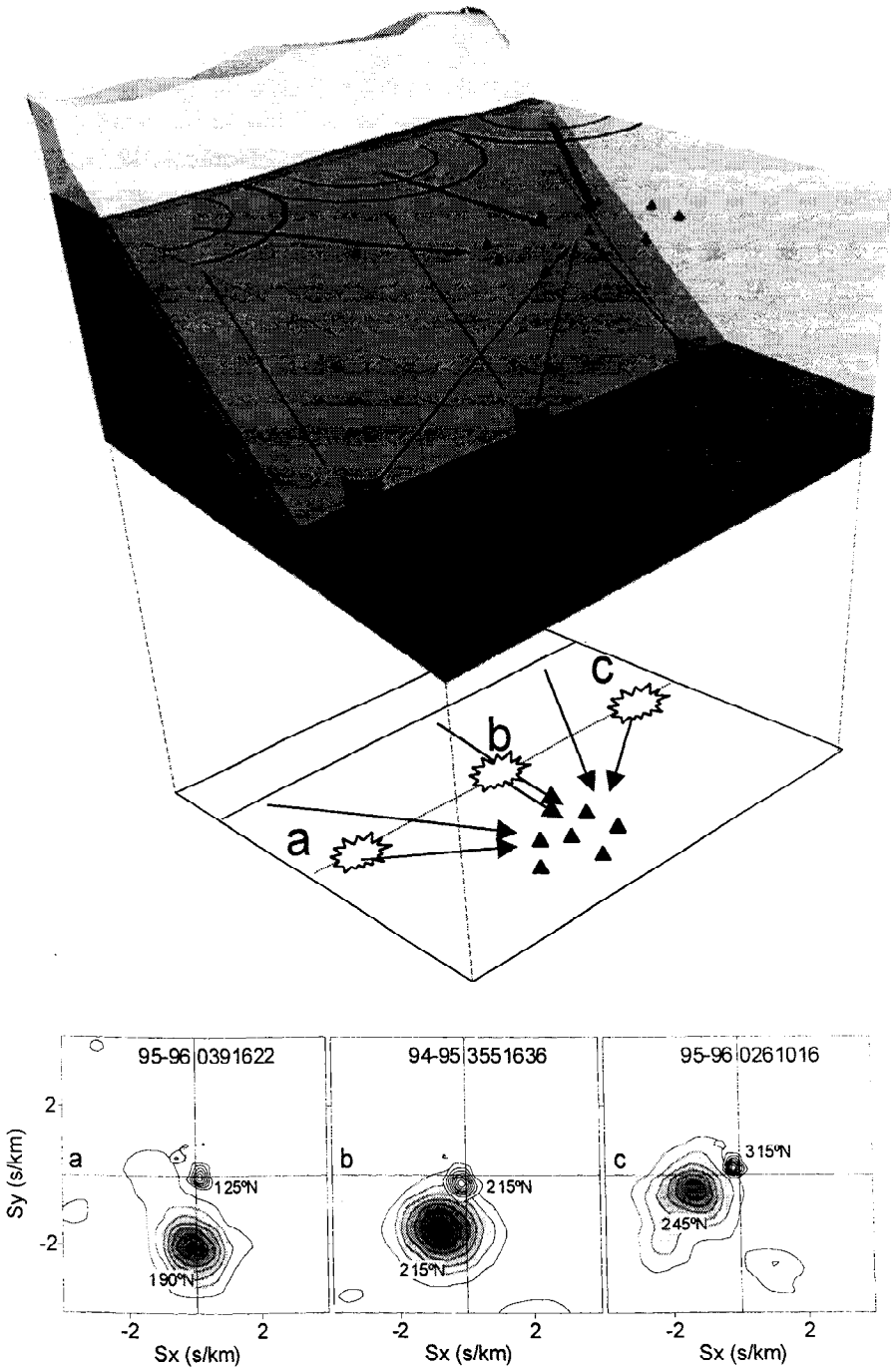

Figure 23. (top) Sketch of the conceptual source model of the LP1 and LP2 events. (bottom) Apparent slowness solutions for three examples of hybrid events. The letters a, b and c correspond to the sources sketched in the top figure. See text for details.

In Chouet's calculations the width-to-length ratio, *W/L*, is fixed to 0.5. As noted by *Ferrazzini et al.* [1990], the dependence of the dispersion characteristics on the value of *W/L* is small and will not be considered in our discussion.

9.3.2. Crack dimensions. The first step to constrain the dimensions of the seismovolcanic LP1 and LP2 sources is to determine the frequency of the spectral peaks observed in the spectra. We stacked the array-averaged spectra of 24 LP1 and low-frequency tremor samples and 32 LP2 events and selected eight peaks, shown in Table 4. The second step is to check whether the observed distribution of spectral peaks is compatible with the modes of resonance of a fluid-filled crack. On the basis of the geological observations we assumed that our source is a crack filled with water containing a small gas volume fraction, due to the shallowness of the source and the existence of fumarolic systems in the area.. Thus the parameters of the model are supposed to be v_s=1.5 km/s, v_f=0.5 km/s, ρ_s=2.5 g/cm^3, and ρ_f=1.0 g/cm^3 [*Nakano et al.*, 1998]. If we suppose that the Lamé constants are equal, then

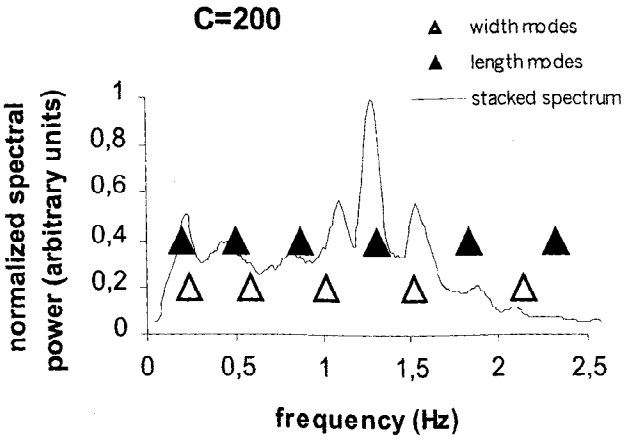

Figure 24. Average of 24 array-averaged LP1 and low-frequency tremor spectra, showing the presence of several spectral peaks in the low-frequency band. Symbols mark the frequency of the peaks predicted by the fluid-filled crack model, using the parameters of Table A1. Solid triangles correspond to length modes and open triangles to width modes.

$$\frac{b}{\mu} = 3\frac{v_f^2 \rho_f}{v_s^2 \rho_s}, \tag{11}$$

whose value is 0.13, in the range calculated by Chouet in his model. Then, using the crack wave dispersion curves $V(\Lambda_L)$, we calculated the frequency of the corresponding spectral peaks for a certain crack geometry by

$$f(\Lambda_L) = \frac{V(\Lambda_L)}{L \cdot \Lambda_L}, \tag{12}$$

The best fit between the calculated frequencies and the appearance of peaks in the data spectra (Figure 24) is obtained for the crack dimensions shown in Table 5. The results show that the LP1 events are compatible with a crack 150 m long and the LP2 events with a crack 70 m long.

9.3.3. Quasi-monochromatic tremor source. As described above, LP3 events and quasi-monochromatic tremor are characterized by a dominant peak followed by its harmonics up to order 8 (Figure 25). This spectral pattern is a clear source effect, because it is observed only for these kinds of events. As mentioned previously, the simplest model that can fit this kind of observation is a degassing process in an open cylindrical conduit,

Table 4. Frequencies of Main Peaks Observed in the LP1 and LP2 Spectra

LP1 (Hz)	LP2 (Hz)
0.2	0.3
0.5	0.8
0.8	1.5
1.1	1.7
1.3	1.9
1.5	2.3
1.9	2.7
2.1	3.3

Table 5. Crack Dimensions and Stiffness

	LP1	LP2
L (m)	150	70
W (m)	120	50
d (cm)	10	2
C	200	500

L, length; W, width; d, aperture; C, crack stiffness.

for which the length is much greater than the radius, as observed in other volcanoes such as Galeras [*Gil Cruz and Chouet*, 1997]. With this simple assumption the length of the resonator, L, can be estimated from the relationship

$$f = \frac{c}{2L}, \tag{13}$$

where c is the sound speed in the fluid that fills the pipe, and f is the frequency of the fundamental peak. If we assume a

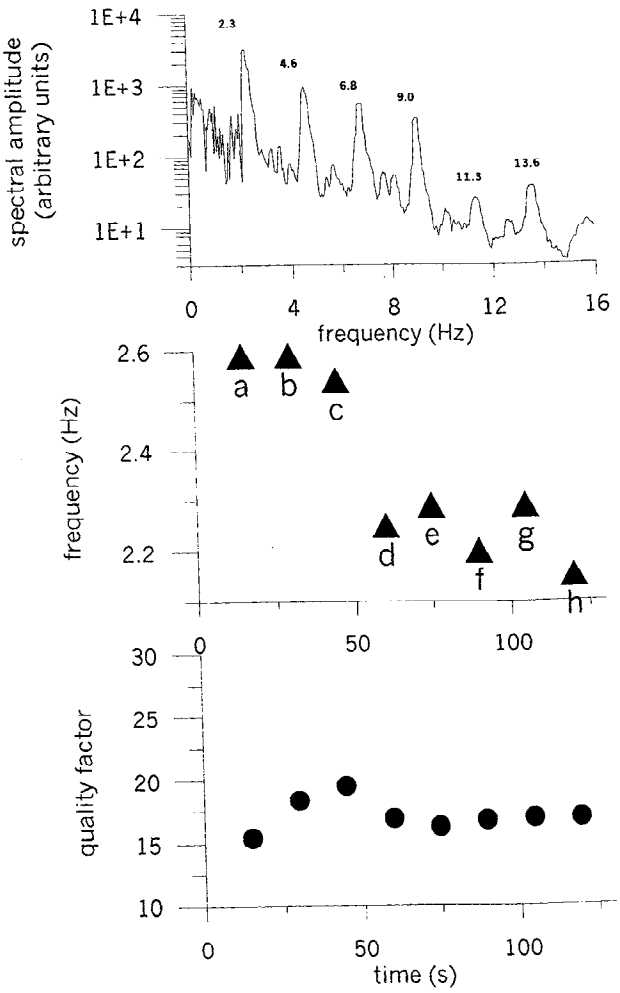

Figure 25. (top) Example of the spectral velocity amplitude of a 10.24 s portion (marked d in the middle figure) of a 150 s sample of quasi-monochromatic tremor. Numbers represent the frequency of the main peaks. (middle) Evolution of the fundamental peak frequency along a tremor episode. (bottom) Evolution of the quality factor of the fundamental peak.

reasonable value for the acoustic velocity in the fluid equal to 0.5 km/s, which corresponds to a bubbly water with a temperature of 200°C, pressure of 2.5 Mpa, and gas/water volume fraction of 1 % and use the first value of the frequency of the fundamental peak at 2.6 Hz, we obtain a value for the pipe length of around 100 m. If we assume that the pipe is filled only by gas, instead of the gas-water mixture, the sound speed should be smaller, which provides a shorter resonator. As reported in Figure 25, in some cases a time variation of the frequency of the fundamental peak is observed along the tremor signal. The peak value ranges between 2.6 Hz at the beginning of the tremor and 2.1 Hz at the end of it. The quality factor associated with these peaks seems to remain stable, around 17 (see Figure 25). A variation of the acoustic properties of the fluid that fills up the conduit and/or a change of the crack dimension could produce the decrease of the frequency of the fundamental peak. Since this variation of the frequency takes place during the same tremor episode, it is more reasonable to assume a variation of the acoustic properties of the fluid. In this case we deduce a decrease of the sound speed between 0.5 km/s at the beginning of the tremor to close to 0.4 km/s at the end, a decrease of around 20%. This change of the properties of the fluid could be related to the change of the gas/water ratio inside the pipe, and/or a depressurization of the gas during the tremor episode. For example, following Kumagai and Chouet, fixing the pressure and temperature at 2.5 Mpa and 200°C, respectively, this decrease of the sound speed would represent an increase of the gas/water ratio between the initial 1% to a value close to 2%.

Although the array analysis of these types of events (LP3 and quasi-monochromatic tremor) provided a source direction similar to those observed for the other volcanic events, the accuracy of the solutions of these types of volcanic events and the absence of evidences in surface of both cracks and pipes do not permit us to relate directly both source mechanisms.

10. Conclusions

Mainly volcano-tectonic earthquakes and volcanic events (long-period events and volcanic tremor) compose the analyzed seismic activity of the Deception Island volcano. VT seismicity evidences the presence of a crack system aligned north-south, located close to the site of the seismic antenna. LP events and volcanic tremor share the same source area. The volcanic tremor appears to be composed of the temporal overlapping of single long-period events. The typical signature of the pure volcanic signals is dominated by an initial high-frequency P wave followed by a complex mixture of low-frequency surface waves. Some events (named hybrids) show a very energetic high-frequency first phase. The wave-field properties of the seismovolcanic signals are compatible with the existence of a shallow fluid-filled crack system at a depth of some hundreds of meters. The differences observed in the back azimuth between low and high frequencies are interpreted as the near-field effect, in association to the resonance of a nonvertical crack. This near-field effect permits us also to observe the evolution of the resonance phenomena. A few episodes of the degassification process in an open conduit were observed and modeled with a simple organ pipe resonator, obtaining a similar linear dimension of the cracks to those obtained above.

The seismic activity recorded at Deception Island between 1994 and 1997 is compatible with some of the geological and geophysical features (the existence of several fracture systems, a shallow aquifer, and hot materials at shallow depth) of the island, as the response of a reasonably stable stationary geothermal process. The model and observations provide a background information that will be useful for the correct interpretation of the future evolution of the volcanic activity of the island.

Appendix: Covariance Matrix

The covariance matrix in the time domain is defined by [*Jurkevics*, 1988]

$$S_{ij} = \frac{1}{N}\sum_{k=1}^{N} A_i^k A_j^k , \qquad (A1)$$

where A_i and A_j are two orthogonal components of the same 3-D station. Both indices i and j (1, 2, 3) correspond to x, y and z components (or east-west, north-south, and vertical respectively). In the following we refer to the eigenvalues having the order relation $\lambda_1 \geq \lambda_2 \geq \lambda_3$ and to the corresponding eigenvectors as $\mathbf{v_i}$. We compute the particle motion rectilinearity by

$$RL = 1 - \frac{\lambda_2 + \lambda_3}{2\lambda_1}, \qquad (A2)$$

RL takes values between 0 (spherical motion) and 1 (rectilinear motion). We define the polarization vector $\boldsymbol{P}$ as a vector having the same direction of the eigenvector $\mathbf{v}_1$, vertical component positive (i.e., above the Earth surface), and unitary modulus (Figure A1). The angle between $\boldsymbol{P}$ and the z axis is named β. We use the unitary wave vector $\boldsymbol{k}$, whose horizontal components are obtained through the array analysis. The vertical component of $\boldsymbol{k}$ is computed by the incidence angle α, being $\alpha = arcsin(s\ v)$ where s is the apparent slowness obtained by the array analysis and v is fixed at 1 km/s, derived from the model reported in Table A1, averaging the velocity in the shallowest layers. The angles γ (between $\boldsymbol{P}$ and $\boldsymbol{k}$) and ψ (between the projection of $\boldsymbol{P}$ on the x-y plane and north) are then computed through dot products. All of these parameters are needed to distinguish between different kinds of waves.

The analysis described above works well with direct P waves, but for secondary waves, there is a problem in the estimation of α, because the different types of waves have different velocities. For this reason we compute two wave vectors $\boldsymbol{k}_p$ and $\boldsymbol{k}_s$, the

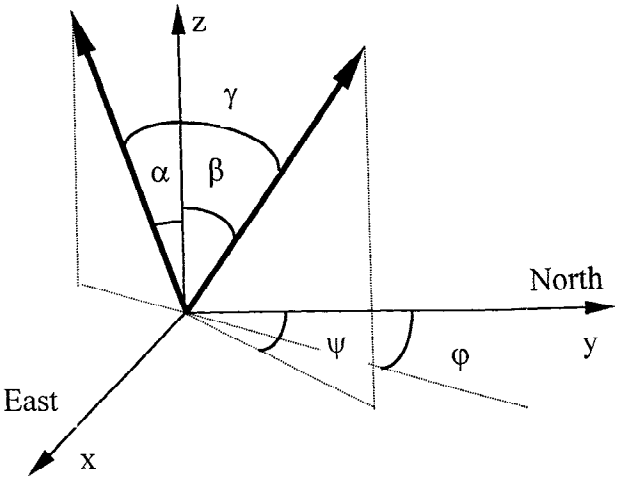

Figure A1. Representation of the polarization and wave vectors discussed in the covariance matrix analysis.

Table A1.Covariance Matrix Parameters Expected for Different Type of Seismic Waves

Seismic Wave	RL	β	γ	ψ−φ
P	1	α	0°	0°
S	1		90°	
SV	1	90°-α	90°	0°
SH	1	90°	90°	90°
Rayleigh	~0.5	0°	90°	0°
Love	1	90°	90°	90°

RL, rectilinearity; β, the angle between polarization vector and z axis; γ, angle between polarization and wave vectors; ψ-φ, explained in Figure A1.

former using the P-wave velocity v_p=v and the latter using the S-wave velocity v_S=$v/1.73$. Consequently, we estimate two values of the incidence angle, α_p and α_s, and two values of γ, γ_p, and γ_s. Once both angles (γ_p and γ_s) are estimated for both wave velocities (v_p and v_S), if the incoming wave is a true P wave, γ_p should be close to 0° and γ_s could have any value. If the incoming wave were a true S or other type of wave, then γ_p could have any value, and γ_s should be close to 90°. When we calculate the average $(\gamma_p+\gamma_s)/2$, if it is less than 45°, we are observing a predominant P-wave arrival ($\gamma=\gamma_p$ and $\boldsymbol{k}=\boldsymbol{k}_p$), otherwise we are observing an S-wave or surface wave arrivals ($\gamma=\gamma_s$ and $\boldsymbol{k}=\boldsymbol{k}_s$).

Acknowledgments. We gratefully acknowledge the useful comments of Bernard Chouet, Marcello Martini and José Morales. Alan Linde, John C. Lahr and an anonymous reviewer offered very helpful suggestions that permitted us to improve the paper. Enrique Carmona and Carmen Martínez helped us to elaborate the final version of this paper. This research has been partially supported by the projects ANT95-0994-C03-02 and ANT98-1111, by italian G.N.V.- CNR, and by the Grupo de Investigación en Geofísica de la J.A. RNM104. We would like to thank the Spanish Army and Navy for providing us with logistical help during the Antarctic surveys in the "Gabriel de Castilla" station.

References

Aki, K., M. Fehler, and S. Das, Source mechanism of volcanic tremor: Fluid-driven crack models and their application to the 1963 Kilauea eruption, *J. Volcanol. Geotherm. Res.*, *2*, 259-287, 1977.

Aki, K., and R. Koyanagi, Deep volcanic tremor and magma ascent mechanism under Kilauea, Hawaii, *J. Geophys. Res.*, *86*, 7095-7109, 1981.

Alguacil, G., J. Almendros, E. Del Pezzo, A. García, J.M. Ibáñez, M. La Rocca, J. Morales, and R Ortiz, Observations of volcanic earthquakes and tremor at Deception Island, Antarctica, *Ann. Geofis.*, *42*, 417-436, 1999.

Almendros, J., J.M. Ibáñez, G. Alguacil, E. Del Pezzo, and R. Ortiz, Array tracking of the volcanic tremor source at Deception Island, Antarctica, *Geophys. Res. Lett.*, *24*, 3069-3072, 1997.

Almendros, J., J.M. Ibáñez, G. Alguacil, and E. Del Pezzo, Array analysis using circular wave-front geometry: An application to locate the nearby seismo-volcanic source, *Geophys. J. Int.*, *136*, 159-170, 1999.

Almendros, J., J.M. Ibáñez, G. Alguacil, J. Morales, E. Del Pezzo, M. La Rocca, R. Ortiz, V. Araña, and M.J. Blanco, A double seismic antenna experiment at Teide Volcano: Existence of local seismicity and lack of evidences of volcanic tremor. *J. Volcanol. Geotherm. Res.*, in press, 2000.

Aristarain, A.J., and R.J. Delmas, Ice record of a large eruption of Deception Island volcano (Antarctica) in the XVIIth century, *J. Volcanol. Geotherm. Res.*, *80*, 17-25, 1998.

Baker, P., Deception Island, in *Volcanoes of the Antarctic Plate and Southern Oceans*, edited by W. LeMasurier, J. Thomson, pp. 316-321, *Antarc. Res. Ser.*, vol. *48*, AGU, Washington, D. C., 1990.

Baker, P., D. Phil, M. McReath, M. Harvey, M. Roobol, and T. Davies, The geology of the South Shetland Islands, V, volcanic evolution of Deception Island, *Br. Antarct. Surv. Sci. Rep.*, *78*, 1975.

Bianco, F., M. Castellano, G. Milano, and G. Vilardo, Shear-wave polarization alignment on the eastern flank of Mt.Etna volcano (Sicily, Italy), *Ann. Geofis.*, *39*, 429-443, 1996.

Casertano, L., Volcanic activity at Deception Island, in *Antarctic Geology*, pp. 33-47 Sci. Comm. on Antarct. Res, London, 1967.

Chouet, B., Excitation of a buried magmatic pipe: A seismic source model for volcanic tremor, *J. Geophys. Res.*, *90*, 1881-1893, 1985.

Chouet, B. A., Dynamics of a fluid-driven crack in three dimensions by the finite difference method, *J. Geophys. Res.*, *91*, 13967-13992, 1986.

Chouet, B., Resonance of a fluid-driven crack: radiation properties and implications for the source of long-period events and harmonic tremor, *J. Geophys. Res.*, *93*, 4375-4400, 1988.

Chouet, B., A seismic model for the source of long-period events and harmonic tremor, in *Volcanic Seismology*, edited by K.Aki, P. Gasparini, and R. Scarpa, pp. 133-156, Springer-Verlag, Berlin, 1992.

Chouet, B., Long-period volcano seismicity: its source and use in eruption forecasting, *Nature*, *380*, 309-316, 1996.

Chouet, B., G. Saccorotti, M. Martini, P. Dawson, G. De Luca, G Milana, and R. Scarpa, Source and path effects in the wave fields of tremor and explosions at Stromboli Volcano, Italy, *J. Geophys. Res.*, *102*, 15,129-15,150, 1997.

Correig, A. M., M. Urquizu, J. Vila, and J. Marti, Analysis of the occurrence of seismicity al Deception Island (Antarctica). A nonlinear approach, *Pure Appl. Geophys.*, *149*, 553-574, 1997.

Crosson, R. S., and D.A. Bame, A spherical source model for low-frequency volcanic earthquakes, *J. Geophys. Res.*, *90*, 10237-10247, 1985.

De Rosa, R., R. Mazzuoli, R.H. Omarini, G. Ventura, and J.G. Viramonte, A volcanological model for the historical eruptions at Deception Island (Bransfield Strait, Antarctica), *Terra Antart.*, *2*, 95-101, 1995.

Del Pezzo, E., C. Godano, A. Gorini, and M. Martini, Wave polarization and location of the source of the explosion quakes at Stromboli volcano, in *Volcanic Seismology*, edited by K.Aki, P. Gasparini, and R. Scarpa, pp. 279-296, Springer-Verlag, Berlin, 1992.

Del Pezzo, E., M. La Rocca, and J.M., Ibáñez, Observations of high-frequency scattered waves using dense arrays at Teide volcano, *Bull. Seismol. Soc. Am.*, *87*, 1637-1647, 1997.

Ferrazzini, V., and K. Aki, Preliminary results from a field experiment on volcanic events at Kilauea using an array of digital seismographs, in *Volcanic Seismology*, edited by K.Aki, P. Gasparini, and R. Scarpa, pp. 168-189, Springer-Verlag, Berlin, 1992.

Ferrazzini, V., B. Chouet, M. Fehler, and K. Aki, Quantitative analysis of long-period events recorded during hydrofracture experiments at Fenton Hill, New Mexico, *J. Geophys. Res.*, *95*, 21871-21884, 1990.

Ferrazzini, V., K. Aki, and B.A. Chouet, Characteristics of seismic waves composing Hawaiian volcanic tremor and gas-piston events observed by a near-source array, *J. Geophys. Res.*, *96*, 6199-6209, 1991.

Fehler, M., Observations of volcanic tremor at Mount St. Helens volcano, *J. Geophys. Res.*, *88*, 3476-3484, 1983.

Frankel, A., S. Hough, P. Friberg, and R. Busby, Observations of Loma Prieta aftershocks from a dense array in Sunnyvale, California, *Bull. Seismol. Soc. Am.*, *81*, 1900-1922, 1991.

Gil Cruz, F., and B.A. Chouet, Long-period events, the most characteristic seismicity accompanying the emplacement and extrusion of a lava dome in Galeras volcano, Colombia, in 1991, *J. Volcanol. Geotherm. Res.*, *77*, 121-158, 1997.

Goldstein, P., and B.A. Chouet, Array measurements and modeling of sources of shallow volcanic tremor at Kilauea volcano, Hawaii, *J. Geophys. Res.*, *99*, 2637-2652, 1994.

González Ferrán, O., *Volcanes de Chile*, Inst. Geogr. Mil., Santiago de Chile 1995.

González Ferrán, O., and Y. Katsui, Estudio integral del volcanismo cenozoico superior de las islas Shetland del Sur, Antártica, *Inst. Antarct. Chileno Ser. Cient.*, *1*, 123-174, 1970.

Hawkes, D., Geology of the South Shetland Islands II. The geology and petrology of Deception Island, *Falkland Isl. Dependencies Surv. Sci. Rep.*, *27*, 1961.

Ibáñez, J. M., J. Morales, G. Alguacil, J. Almendros, R. Ortiz, and E. Del Pezzo, Intermediate-focus earthquakes under South Shetland Islands (Antarctica), *Geophys. Res. Lett.*, *24*, 531-534, 1997a.

Ibáñez, J. M., J. Morales, G. Alguacil, J. Almendros, R Ortiz, E. Del Pezzo, A. Posadas, and F. Luzón, Actividad sísmica regional alrededor de las islas Livingston y Decepción entre 1992 y 1996: Terremotos superficiales y profundos, *Bol. RSEHN*, *93*, 93-101, 1997b.

Jurkevics, A., Polarization analysis of three-component array data, *Bull. Seismol. Soc. Am.*, *78*, 1725-1743, 1988.

Kanasewich, E. R., *Time sequence analysis in geophysics*, Univ. of Alberta Press, Edmonton, 1981.

Lahr, J., B.A. Chouet, C. Stephens, J. Power, and R. Page, Earthquake classification, location and error analysis in a volcanic environment: Implications for the magmatic system of the 1989-1990 eruptions at Redoubt volcano, Alaska, in *The 1989-1990 eruptions of Redoubt volcano, Alaska*, edited by T. Miller, and B.A. Chouet, *J. Volcanol. Geotherm. Res.*, *62*, 137-151, 1994.

Marti, J., and A. Baraldo, Pre-caldera pyroclastic deposits of Deception Island (South Shetland Islands), *Antar. Sci.*, *2*, 345-352, 1990.

Martini, M., and L. Giannini, Deception Island (South Shetlands): An area of active volcanism in Antarctica, *Mem. Soc. Geol. It.*, *43*, 117-122, 1988.

Mètaxian, J. P., P. Lesage, and J. Dorel, Permanent tremor of Masaya volcano, Nicaragua: Wave field analysis and source location, *J. Geophys. Res.*, *102*, 22,529-22,545, 1997.

Nakano, M., H. Kumagai, M. Kumazawa, K. Yamaoka, and B.A. Chouet, The excitation and characteristic frequency of the long-period volcanic event: An approach based on an inhomogeneous autoregressive model of a linear dynamic system, *J. Geophys. Res.*, *103*, 10,031-10,046, 1998.

Ortiz, R., et al., Monitoring of the volcanic activity of Deception Island, South Shetland Islands, Antarctica (1986-1995), in *The Antarctic Region: Geological Evolution and Processes*, edited by C.A. Ricci, pp. 1071-1076, Terra Antarctica Publ., Siena, 1997.

Roobol, M. J., A model for the eruptive mechanisms of Deception Island from 1820 to 1970, *Br. Antarct. Surv. Bull.*, *49*, 137-156, 1979.

Saccorotti, G., B.A. Chouet, M. Martini, and R. Scarpa, Bayesian statistics applied to the location of the source of explosions at Stromboli Volcano, Italy, *Bull. Seismol. Soc. Am.*, *88*, 1099-1111, 1998.

Seidl, D., and M. Hellweg, Volcanic tremor recordings: polariztion analysis, in *Volcanic tremor and magma flow*, edited by R. Schick, and R Mugiono, pp. 31-46, Forschungszentr., Jülich, Germany, 1991.

Smellie, J. L., Recent observations on the volcanic history of Deception Island, South Shetland Islands, *Br. Antarct. Surv. Bull.*, *81*, 83-85, 1988.

Smellie, J. L., Deception Island, in *Tectonics of the Scotia Arc, Antarctica*, edited by I. Dalziel, AGU, Washington, D.C., 1989.

Smellie, J. L., R.J. Pankhurst, M.R. Thomson, and R.E. Davies, The geology of the South Shetland Islands: stratigraphy, geochemistry and evolution, *Br. Antarct. Surv. Bull.*, *81*, 83-85, 1988.

Vila, J., J. Marti, R. Ortiz, A. Garcia, and A.M. Correig, Volcanic tremors at Deception Island (South Shetland Islands, Antarctica), *J. Volcanol. Geotherm. Res.*, *53*, 89-102, 1992.

Vila, J., A.M. Correig, and J. Marti, Attenuation and source paramcters at Deception Island (South Shetland Islands, Antarctica), *Pure Appl. Geophys.*, *144*, 229-250, 1995.

J. Almendros, G. Alguacil, and J.M. Ibáñez, Instituto Andaluz de Geofísica, Universidad de Granada, Campus de Cartuja s/n, 18071 Granada, Spain. (alm@iag.ugr.es; alguacil@iag.ugr.es; ibanez@iag.ugr.es)

E. Del Pezzo and M. La Rocca, Osservatorio Vesuviano, Via Diocleziano 328, 80124 Napoli, Italy. (delpezzo@osve.unina.it; mlarocca@osve.unina.it)

A. García and R. Ortiz, Museo nacional de Ciencias Naturales, Dpto. Volcanología, C/ José Gutiérrez Abascal, nº 2, 28006 Madrid, Spain. (aliciag@mncn.csic.es; mcnro514@mncn.csic.es)

(Received March 30, 1999; revised November 18, 1999;
accepted December 23, 1999.)